Microsc. Microanal. 17, 728–751, 2011
doi:10.1017/S1431927611000523

Microscopy AND Microanalysis

Comprehensive Comparison of Various Techniques for the Analysis of Elemental Distributions in Thin Films

D. Abou-Ras,[1,*] R. Caballero,[1] C.-H. Fischer,[1] C.A. Kaufmann,[1] I. Lauermann,[1] R. Mainz,[1] H. Mönig,[1] A. Schöpke,[1] C. Stephan,[1] C. Streeck,[1] S. Schorr,[2] A. Eicke,[3] M. Döbeli,[4] B. Gade,[5] J. Hinrichs,[6] T. Nunney,[7] H. Dijkstra,[8] V. Hoffmann,[9] D. Klemm,[9] V. Efimova,[9] A. Bergmaier,[10] G. Dollinger,[10] T. Wirth,[11] W. Unger,[11] A.A. Rockett,[12] A. Perez-Rodriguez,[13,14] J. Alvarez-Garcia,[15] V. Izquierdo-Roca,[14] T. Schmid,[16] P.-P. Choi,[17] M. Müller,[18] F. Bertram,[18] J. Christen,[18] H. Khatri,[19] R.W. Collins,[19] S. Marsillac,[19] and I. Kötschau[20]

[1]*Helmholtz-Zentrum Berlin für Materialien und Energie, Hahn-Meitner-Platz 1, 14109 Berlin, Germany*
[2]*Free University Berlin, Department for Geosciences, Malteserstr. 74-100, 12249 Berlin, Germany*
[3]*Zentrum für Sonnenenergie- und Wasserstoff-Forschung, Industriestr. 6, 70565 Stuttgart, Germany*
[4]*ETH Zurich, Laboratory of Ion Beam Physiscs, Schafmattstrasse 20, 8093 Zurich, Switzerland*
[5]*Thermo Fisher Scientific, Im Steingrund 4-6, 63303 Dreieich, Germany*
[6]*Thermo Fisher Scientific, Hanna-Kunath Str. 11, 28199 Bremen, Germany*
[7]*Thermo Fisher Scientific, The Birches, Imberhorne Lane, East Grinstead, West Sussex, RH19 1UB, UK*
[8]*Thermo Fisher Scientific, Takkebijsters 1, 4817 Breda, The Netherlands*
[9]*IFW Dresden, Helmholtzstraße 20, 01069 Dresden, Germany*
[10]*Universität der Bundeswehr München, LRT2, Werner-Heisenberg-Weg 39, D-85577 Neubiberg, Germany*
[11]*Federal Institute for Materials Research and Testing, Unter den Eichen 87, 12205 Berlin, Germany*
[12]*Department of Materials Science & Engineering, University of Illinois, 1304 W. Green St., Urbana, IL 61801, USA*
[13]*Catalonia Institute for Energy Research (IREC), C. Jardins de les Dones de Negre 1, 08930 Sant Adrià del Besòs (Barcelona), Spain*
[14]*IN²UB, Departament d'Electrònica, Universitat de Barcelona, C. Martí i Franquès 1, 08028 Barcelona, Spain*
[15]*Centre de Recerca i Investigació de Catalunya (CRIC), Trav. de Gràcia 108, 08012 Barcelona, Spain*
[16]*ETH Zurich, Department of Chemistry and Applied Biosciences, 8093 Zurich, Switzerland*
[17]*Max Planck Institute for Iron Research, Max-Planck-Str. 1, 40237 Düsseldorf, Germany*
[18]*Otto-von-Guericke-University Magdeburg, Institute of Experimental Physics, Universitätsplatz 2, 39106 Magdeburg, Germany*
[19]*Center for Photovoltaics Innovation and Commercialization (PVIC), University of Toledo, Toledo, OH 43606, USA*
[20]*centrotherm photovoltaics AG, Technology Thin Film, Johannes-Schmid-Str. 8, 89143 Blaubeuren, Germany*

Abstract: The present work shows results on elemental distribution analyses in $Cu(In,Ga)Se_2$ thin films for solar cells performed by use of wavelength-dispersive and energy-dispersive X-ray spectrometry (EDX) in a scanning electron microscope, EDX in a transmission electron microscope, X-ray photoelectron, angle-dependent soft X-ray emission, secondary ion-mass (SIMS), time-of-flight SIMS, sputtered neutral mass, glow-discharge optical emission and glow-discharge mass, Auger electron, and Rutherford backscattering spectrometry, by use of scanning Auger electron microscopy, Raman depth profiling, and Raman mapping, as well as by use of elastic recoil detection analysis, grazing-incidence X-ray and electron backscatter diffraction, and grazing-incidence X-ray fluorescence analysis. The $Cu(In,Ga)Se_2$ thin films used for the present comparison were produced during the same identical deposition run and exhibit thicknesses of about 2 μm. The analysis techniques were compared with respect to their spatial and depth resolutions, measuring speeds, availabilities, and detection limits.

Key words: elemental distributions, comparison, depth profiling, chemical mapping, thin films, solar cells, chalcopyrite-type, $Cu(In,Ga)Se_2$

Introduction

Thin-film research and development is performed on a broad range of materials and on individual layers with thicknesses ranging from a few nanometers to several micrometers. For all these cases, it is essential to have access to the compositions of the thin films, which may be divided into concentrations of matrix and trace elements. Since the compositions are frequently not distributed homogeneously in thin films, and since these elemental distributions may affect the electrical and optoelectronic properties of thin-film devices considerably, the analysis of elemental distributions in thin films is an important issue in both research and industry (Oechsner, 1984; Reniers & Tewell, 2009). Further comparisons of techniques for elemental distribution analysis have been reported by Ives et al. (1997), Hodoroaba et al. (2001), Bohne et al. (2004), and Escobar Galindo et al. (2009).

In the present work, several techniques providing information on elemental distributions were employed on about

Received November 5, 2010; accepted April 4, 2011
*Corresponding author. E-mail: daniel.abou-ras@helmholtz-berlin.de

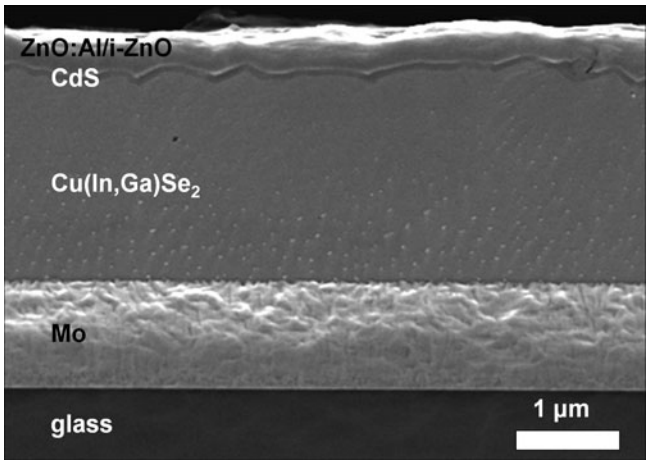

Figure 1. Cross-sectional scanning electron micrograph of the ZnO:Al/i-ZnO/CdS/Cu(In,Ga)Se_2/Mo/glass stack studied for the present work. The solar cell is illuminated from the top.

2 μm thick Cu(In,Ga)Se_2 thin films from the same identical deposition run and the same identical Mo/soda-lime glass substrate. Cu(In,Ga)Se_2 is used as absorber material in thin-film solar cells, leading to solar-conversion efficiencies of up to 20.1% (Jackson et al., 2011). The present work will focus on the elemental distributions of the matrix elements, particularly those of In and Ga. The techniques are compared with respect to their spatial and lateral resolutions, their measuring speeds, their availabilities, and their detection limits.

Materials and Sample Preparation

Cu(In,Ga)Se_2 thin films (2 μm) were coevaporated from elemental sources on Mo-coated (sputtered, 1 μm) soda-lime glass substrates (2 mm) by a three-stage process (Kaufmann et al., 2005), which consists of coevaporation of In, Ga, and Se (stage 1), deposition of Cu and Se until Cu_xSe is formed on top of Cu(In,Ga)Se_2 (stage 2), and again coevaporation of In, Ga, and Se, until Cu_xSe is consumed and the Cu(In,Ga)Se_2 layer is Cu-poor. According to the quasibinary Cu_2Se-In_2Se_3 phase diagram (Herberholz et al., 1999), single-phase $CuInSe_2$ (and also $CuGaSe_2$) is present for Cu concentrations of about 24–24.5 at.%; i.e., Cu(In,Ga)Se_2 is substoichiometric with a certain concentration of Cu vacancies, which are responsible for the *p*-type conductivity.

The Cu(In,Ga)Se_2/Mo/glass stacks analyzed for the present work were produced in the identical deposition runs for Mo sputtering and Cu(In,Ga)Se_2 evaporation. A part of the Cu(In,Ga)Se_2/Mo/glass stacks were further processed toward completed solar cells by depositing a CdS buffer layer (about 50 nm) in a chemical bath and then sputtering a ZnO:Al/i-ZnO bilayer (with thicknesses of about 40 and 500 nm). Finally, a Ni-Al grid was deposited on top of the ZnO:Al/i-ZnO bilayer to facilitate the current collection. The reader is referred to Figure 1 for a scanning electron micrograph of a completed solar cell produced from this stack. The solar cells produced in the identical run as the Cu(In,Ga)Se_2/Mo/glass stacks studied for the present work exhibited a conversion efficiency of 16.1% (average from 21 individual cells with areas of 0.5 cm^2).

Due to substrate rotation during the Cu(In,Ga)Se_2 evaporation, the lateral variations in composition are only about 5 rel.%. The integral compositions of the Cu(In,Ga)Se_2 thin films were determined by X-ray fluorescence analysis (XRF) by use of a Cu(In,Ga)Se_2 standard, sampling the entire 2 μm thick films, and given in Table 1.

In general, In and Ga are not homogeneously distributed in Cu(In,Ga)Se_2 layers; i.e., the Ga concentration is larger close to the Mo back contact. Since Cu and Se are generally found to be distributed homogenously across the Cu(In,Ga)Se_2 layers, the In elemental distribution behaves inversely to that of Ga.

This compositional distribution may be related to differences in Ga-Se/In-Se and Cu-Se bonding lengths. In-Se is much larger than Cu-Se in $CuInSe_2$, whereas Ga-Se is quite similar to Cu-Se in $CuGaSe_2$. Corresponding strain in the Cu(In,Ga)Se_2 solid solution may induce diffusion of In preferentially toward the surface of the growing Cu(In,Ga)Se_2 layer (Gabor et al., 1994). Another possible reason for the formation of the In/Ga gradients in Cu(In,Ga)Se_2 layers may be the smaller formation enthalpy for $CuInSe_2$ than for $CuGaSe_2$ (Cahen & Noufi, 1992). Considering that the final Cu(In,Ga)Se_2 layer first forms by chemical reactions between the Cu_xSe compounds mentioned above and Cu(In,Ga)Se_2 at the surface of the growing thin film (Klenk et al., 1993), this is where the compound with the lower formation enthalpy, i.e., $CuInSe_2$, is preferentially present.

In and Ga distributions in Cu(In,Ga)Se_2 layers have an impact on their optoelectronic properties because the band-gap energy of $CuInSe_2$ is smaller (1.04 eV) than that of $CuGaSe_2$ (1.68 eV) (Alonso et al., 2001). This will be shown by the cathodoluminescence results further below; i.e., the In/Ga distributions affect the absorption behavior of the Cu(In,Ga)Se_2 layer in its volume. Since the local In/Ga concentrations in Cu(In,Ga)Se_2 correlate with the position of the conduction-band minimum, also the band alignment with the *n*-type CdS layer (see Fig. 1) is influenced by the in-depth In and Ga distributions. Dullweber et al. (2000) showed that the open-circuit voltage of a Cu(In,Ga)Se_2 solar cell depends on that band-gap energy that corresponds to the Ga concentration close to the surface. Moreover, these authors found that the short-circuit density of this solar cell relates to the overall minimum of the band-gap energy, i.e., of the Ga concentration across the Cu(In,Ga)Se_2 layer.

Table 1. Integral Composition of the Cu(In,Ga)Se_2 Thin Films Studied for the Present Work, as Obtained by XRF.

[Cu] (%)	[In] (%)	[Ga] (%)	[Se] (%)
23 ± 1	17 ± 1	9 ± 1	51 ± 1

Regarding the tetragonal, chalcopyrite-type crystal structure of $Cu(In,Ga)Se_2$, its lattice constant ratio c/a is proportional to the Ga concentration (Suri et al., 1989); i.e., analyses of the local crystal structure may give information also on the local composition. The corresponding analysis techniques, i.e., Raman spectroscopy, grazing-incidence X-ray diffraction (GI-XRD), and electron backscatter diffraction (EBSD), may be influenced by strain present in the $Cu(In,Ga)Se_2$ layers investigated. Macrostress values for these layers of ten to eighty 10^4 N/m^2 are reported (Chakrabarti et al., 1996, 1997; Witte et al., 2009*a*, 2009*b*). Assuming a Young's modulus for $CuInSe_2$ of about 6.49×10^{10} N/m^2 (Fernández & Wasim, 1990), the corresponding macrostrain can be calculated to about 10^{-5}. The corresponding macrostrain-related errors are substantially smaller than other possible errors for the determination of peak positions in GI-XRD patterns and Raman spectra. However, for the EBSD patterns acquired across individual grains for the present work, the key issue is the microstrain contained in the grains, which may differ considerably from the macrostrain.

It should be noted that the In/Ga gradients in $Cu(In,Ga)Se_2$ layers, formed during the film deposition, are rather stable. For temperatures lower than about 200°C, no substantial change in the In and Ga distributions is expected, which is the case for all characterization techniques applied in the present work. Also the ion bombardment of the $Cu(In,Ga)Se_2$ layers taking place during depth profiling or cross-section polishing does not affect the In/Ga gradients in the about 2 μm thick films. This fact is apparent when comparing results obtained by secondary neutral mass spectroscopy, performed at liquid nitrogen temperatures, and, e.g., secondary-ion mass spectroscopy depth profiling at room temperature, which both exhibit similar Ga/In elemental distributions.

Possible impurities in $Cu(In,Ga)Se_2$/Mo stacks on soda-lime glasses can be traced back to diffusion from these glass substrates, which consist mainly of SiO_2, Na_2O, and CaO. Indeed, Na and O are found to be present in all $Cu(In,Ga)Se_2$ films deposited on Mo-coated soda-lime glass, where Na has an important effect on the charge-carrier density because it may occupy Cu vacancies. Typical Na concentrations in $Cu(In,Ga)Se_2$ films deposited on Mo/soda-lime glass substrates are about 0.1–3 at.% (Niles et al., 1997; Granata & Sites, 1998; Rockett et al., 2000), whereas the integral oxygen concentration is assumed to be substantially lower.

Cross-section samples were produced from a part of the $Cu(In,Ga)Se_2$/Mo/glass stacks in the following way. Two stripes of a sample were glued together face-to-face by use of an epoxy glue. Slices were cut from this stack, and their cross sections were polished mechanically and also by means of an Ar-ion polishing machine (BALTEC RES-100, at ambient temperature), using 5 kV and 2 mA at a flat incidence angle of 4°. One part of the cross sections was coated by a very thin (4–5 nm) graphite layer, the other part by a thin (1–2 nm) gold film. For transmission electron microscopy analysis, the slices were mechanically polished down to thicknesses of about 10–15 μm, glued on Mo support rings and then Ar-ion-polished until they were transparent for the electron beam.

Methods and Results

This section describes the individual techniques employed for measuring the matrix elements distributions in $Cu(In,Ga)Se_2$ thin films and the results obtained. It will be divided into results obtained by (destructive) depth profiling and "nondestructive" techniques, both measured from the top side of the $Cu(In,Ga)Se_2$/Mo/glass stack, and into those acquired on cross-section samples. We described those techniques that we consider not broadly known in more detail. The descriptions of rather established methods are kept short. We included explanatory schematics and raw data of the measurements where appropriate.

Depth-Profiling Techniques

Secondary Ion Mass Spectrometry

Secondary ion-mass (SIMS) analysis was conducted in a Cameca IMS 5f instrument with a magnetic sector mass analyzer. Secondary ions were accelerated to an energy of 4,450 eV, energy and mass analyzed, and detected by an electron multiplier or Faraday cup. The sputtering ions were Cs^+ and struck the sample at an energy of 17 keV. The sputtering beam was about 20 μm diameter and was scanned across a 250×250 μm area, producing a uniform square crater in the sample. The sputtering ion beam strikes the sample surface at an angle of 30° with respect to the surface normal. The secondary ion yields were obtained by comparison with other analysis techniques reported here and with reference to compositions obtained by energy-dispersive X-ray (EDX) spectrometry in scanning electron microscopy (see also the Energy-Dispersive X-Ray Spectrometry in a Scanning Electron Microscope subsection below). The total composition is normalized to 100 at.% for the matrix elements. This normalization results in increased noise in the experimental data. Under ideal measurement conditions, transitions of about 10 nm per decade of signal change can be obtained with the Cs^+ ion beam. The depth scale was calibrated by measurement of SIMS crater depths using a Tencor Alpha Step microprofilometer.

A primary advantage of the SIMS technique is its high sensitivity to trace impurities. Mass spectra and depth profiles obtained on this sample showed the presence of common alkali metals including K and Na present throughout the sample and Ca present on the surface but decreasing by two orders of magnitude by about 1 μm deep into the sample. Other impurities in the sample studied included Al and Li (the latter is not commonly observed) as well as O. Ion yields for all electropositive species show clear rises where oxygen is present. Carbon is commonly found and B may be present in some samples. Other impurities are rare. The resulting profiles determined by SIMS and the other depth-profiling techniques are shown in Figure 2.

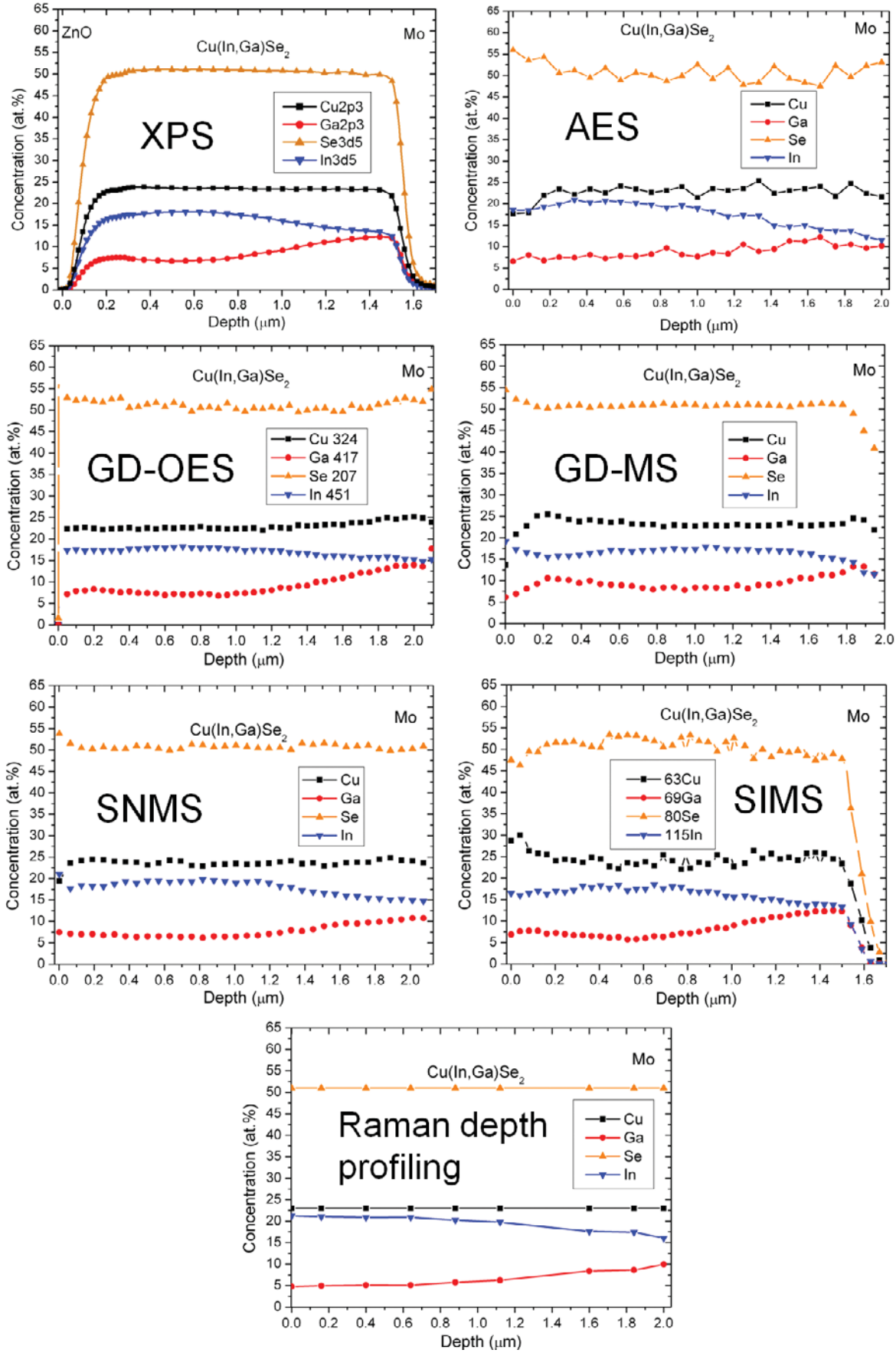

Figure 2. Elemental distributions acquired by means of depth-profiling techniques.

Sputtered Neutrals Mass Spectrometry

Sputtered neutrals mass spectrometry (SNMS) investigations were carried out in a LHS10 system with a SSM 200 module using a quadrupole mass filter. Sputtered neutral particles are post-ionized by electrons with energies of 70 eV (electron-beam SNMS). For sputter erosion, the samples are bombarded by a focused 5 keV Ar^+ ion beam at 60° to the surface normal, scanned across an area of 3×2 mm^2. For enhanced depth resolution, sputtered ions/neutrals from the crater walls are suppressed by electronic gating. During analysis, the samples were cooled with liquid nitrogen to reduce surface roughening by Ar etching. Without cooling, significant surface roughening occurs, causing a distortion of the depth profiles. Sensitivity factors for the quantification of elements in Cu(In,Ga)Se_2 absorbers by SNMS are well known from earlier calibrations by means of EDX and XRF. To compensate for small changes due to instrumental effects, each elemental distribution profile is fitted to the integral elemental concentration as measured by means XRF (Table 1).

SNMS allows an easy and accurate quantification in sputter depth profiling. The reasons are that, for most compounds, more than 98% of sputtered particles are neutrals, and that the post-ionization efficiency by electron impact is independent of the sample composition. Therefore, the sensitivity factors for the elements are—to a first approximation—fixed values. Due to this separation of particle emission and ionization process, matrix effects as known from SIMS analysis, especially by sputtering with Ar ions, are negligible. As the detection limit for SNMS is in the range of 0.05 at.%, simultaneous SIMS measurements are performed for the detection of trace elements of down to 1 ppm. For example, the incorporation of Na in Cu(In,Ga)Se_2 can additionally be detected and roughly quantified by SIMS. In the present work, only the quantitative results from SNMS for the matrix elements in the Cu(In,Ga)Se_2 thin film are shown.

The information depth of SNMS and SIMS is only one to three atomic layers and thus extremely low, compared with other methods presented in this comparison. The depth resolution is in the range of several nm depending on the sputter conditions, the depths of the sputter craters, and the material properties. For Cu(In,Ga)Se_2 solar cells, the depth resolution is often limited by the roughness of the layers analyzed, especially of the polycrystalline Cu(In,Ga)Se_2 absorber.

X-Ray Photoelectron Spectrometry

The X-ray photoelectron spectrometry (XPS) analysis of the sample was performed using a Thermo Scientific K-Alpha spectrometer (Thermo Fisher Scientific, East Grinstead, UK). Photoelectrons were excited by means of a monochromated Al-Kα X-ray source with a photon energy of 1,486.6 eV. The analysis area on the sample is defined by the size of the X-ray spot at the surface, and a spot size of 150 μm was used in the present work (the spot size is defined by the distance traveled across a Cu knife edge, where the XPS signal intensity changes from 20–80%). The X-ray power was 22 W. The kinetic energy of the photoelectrons was measured using a 180° hemispherical analyzer fitted with a 128-channel detector, operated in constant analyzer-energy mode with a pass energy of 150 eV for the individual elemental spectra. This enables the analyzer to operate in "snapshot mode," allowing more rapid acquisitions. In the present experiments, each spectral range of about 20 eV was collected during 5 s. The sample was depth profiled, and so XPS acquisition was interspersed with Ar^+ ion bombardment to remove surface layers. A 2 kV ion energy was used, which had a beam current of 2 μA, rastered across a 2×4 mm^2 area. The sample was mounted on a rotating sample stage to provide a homogeneous etching. Data were collected and processed using the Thermo Scientific Avantage data system. The data were corrected for the lens-transmission function, and background subtraction was performed using a Shirley function calculated from a numerical iterative method. Each element concentration was obtained by dividing calculated peak areas by the corresponding Scofield cross section. Etch rates were calibrated against the known thin-film stacking sequence obtained using EDX in scanning electron microscopy (see description in the Energy-Dispersive X-Ray Spectrometry in a Scanning Electron Microscope subsection further below).

The strength of the XPS technique lies in its ability to quantify both, elemental and chemical state information, from the top 10 nm or less of the surface of a sample. By using ion beam etching, surface layers can be slowly removed, at a rate that is comparable with the probe depth of the XPS technique. This allows profiles to be built up that have good depth resolution and rich information content on the elements present and the chemical environment in which they reside. This makes XPS a powerful technique for examining the chemistry at the interfaces of multilayer devices such as solar cells, where the interaction between adjoining compounds can be of marked contrast to the bulk (in XPS terms) of the layer. These interactions can have significant influence on the ultimate performance of the device.

Auger Electron Spectrometry

The combination of Auger electron spectroscopy (AES) as a surface sensitive technique, providing information from the uppermost few nanometers of the sample, with Ar-ion sputtering enables us to detect the depth distribution of elements in the sample. For quantitative analysis, matrix effects that influence the Auger sensitivity of elements in dependence on the surrounding material have to be taken into account. Possible changes of the sample composition at the surface due to Ar ion sputtering have to be corrected. Furthermore, Ar-ion bombardment may lead to depth-profile distortions due to surface roughening and/or compositional intermixing.

The Auger spectra were acquired at a primary electron energy of 5 keV in the dN/dE mode with a modulation voltage of 4 V and lock-in detection. The electron beam was scanned across an area of 100 μm $\times$ 100 μm. The electron

energy analyzer was a PHI Mod. 15-155 cylindrical mirror analyzer. Ar-ion sputtering was performed by use of 4 keV Ar^+ ions at an angle of incidence of about 50° with respect to the surface normal. Quantification was performed by relating the averages of the signal intensity distributions to the integral concentrations given in Table 1.

By means of AES, it is possible to determine chemical states of the elements. Due to the small information depth of about 1–3 nm, buried interface layers may be detected when AES is combined with sputter depth profiling. The knowledge about composition at interfaces of multilayer systems is important for the optimization of the performance of devices as the solar cells studied for the present work.

Glow-Discharge Optical Emission Spectrometry

The glow discharge optical emission spectrometry (GD-OES) represents a rapid depth-profiling technique capable of qualitative and quantitative elemental analysis of bulk and layered samples (Payling & Jones, 1993; Bengtson, 1994; Angeli et al., 2003). The sample atoms are sputtered in the glow discharge cell under voltages of 600–1,500 V in the atmosphere of inert gas (usually argon). Then, they are excited by plasma species and emit light of certain wavelengths. This characteristic emission is detected by a spectrometer.

The glow discharge can be powered by direct current (dc) or by radio frequency (rf) voltage in a continuous or pulsed mode. By means of rf discharge, also nonconducting samples can be analyzed. The rf mode is more often applied for thin-film analysis, e.g., because of less intense plasma ignition.

For the analysis of nearly all elements (including light elements H, C, N, O) in the films of 1 nm up to more than 100 μm thickness, GD-OES has shown its advantages of high depth resolution (5–10% of layer thickness for layers with thicknesses >3 nm), high sensitivity (0.1–100 μg/g), and high dynamic range (μg/g up to main components). The crater shape and consequently the depth resolution must be optimized by variation of the discharge parameters (rf voltage, Ar gas pressure, pulse frequency, and duty cycle). The easy application of GD-OES is caused by the experimental simplicity (e.g., no ultrahigh vacuum is required) and results in high sample throughput.

The disadvantage of the method is low lateral resolution restricted by the anode diameter. To reduce contaminations of water and hydrocarbons absorbed at inner walls of the glow discharge source and the sample surface, low evacuation pressure ($p_e = 1 \times 10^{-5}$ mbar) and a low leakage rate (3.9×10^{-6} mbar L/s) were used. Before each measurement, the discharge cell was evacuated (30 s) and flushed with pure argon gas (30 s).

The GD-OES analysis of the $Cu(In,Ga)Se_2$ sample was carried out using a Spectruma GDA 750 spectrometer equipped with a 4-mm Grimm-type rf source. As a power supply the Spectruma free running rf generator (6.7 MHz) was used in the regime of constant voltage and pressure (800 V, 1.8 mbar). When brittle samples with low heat conductivity (i.e., glass) are analyzed, softer conditions are needed. In such cases, a pulsed rf discharge may be applied to reduce the introduced power per time. In the present work, pulsed rf discharge was used because of the glassy substrate (pulse frequency 1,222 Hz and duty cycle 4%). The measuring duration for the $Cu(In,Ga)Se_2$/Mo stack was 750 s.

The characteristic emission was detected by means of a Spectruma Paschen-Runge type polychromator (2,400 grooves per mm, 750 mm diameter of the Rowland circle, resolution 0.02 nm) and an Ocean Optics S2000 CCD spectrometer (wavelength: 200–1,100 nm, resolution 0.5 nm). The used emission lines were 207.478 nm (Se), 324.754 nm (Cu), 379.734 nm (Mo), 417.204 nm (Ga), 450.094 nm (In), 588.995 nm (Na), where the Mo and Na signals are not shown in the present work. Enhanced Na signals are found in the Mo layer and at the Mo/glass interface. Quantification of Cu, In, Ga, and Se signals was performed by relating the averages of the signal intensity distributions to the integral concentrations given in Table 1.

Glow-Discharge Mass Spectrometry

The Thermo Scientific ELEMENT GD used in this study is a double-focusing high-resolution mass spectrometer, which features a fast flow GD DC source using argon carrier gas flows of about 400 mL/min. The combination of detectors allows measurements of ultra traces up to matrix elements over a linear dynamic range of 12 orders of magnitude (from 0.2 to larger than 10^{12} counts/s for the matrix signal). Ultra traces and matrix elements can be measured within a single analysis because the detection system switches between detection modes within 1 ms. Typical sensitivities are on the order of 10^{10} counts/s for the matrix signal. The main components of the glow discharge mass spectrometry (GD-MS) are sample holder, plasma chamber, ion optic assembly, magnet, electrostatic analyzer, and detection system. As for GD-OES, the sample (approximately 20 mm diameter) acts as a cathode, and a differential potential is generated between the anode and the cathode in the plasma chamber. Owing to the high electric field in the sample surface, Ar ions are accelerated toward the sample surface, and various kinds of ionization processes occur. The sample ions are then accelerated and focused before entering the magnetic field. They are separated by the analyzer according to their ratios M/z (mass of the element divided by its charge). The intensity of the element signal relative to the matrix signal allows for quantification of the concentration of each element.

The discharge current, gas flow, and voltage were adjusted to achieve sufficient signal intensity (of the order of 10^7 counts/s for the matrix signal), while using soft sputter conditions (lower discharge current compared with bulk analyses) to achieve a good depth resolution. The sputter rate for the experiment is about 5 nm/s. As the present study focuses on the depth profile of matrix components, only the most sensitive low-resolution mode was used. Any possible interference can be neglected in view of the much more intense matrix signals.

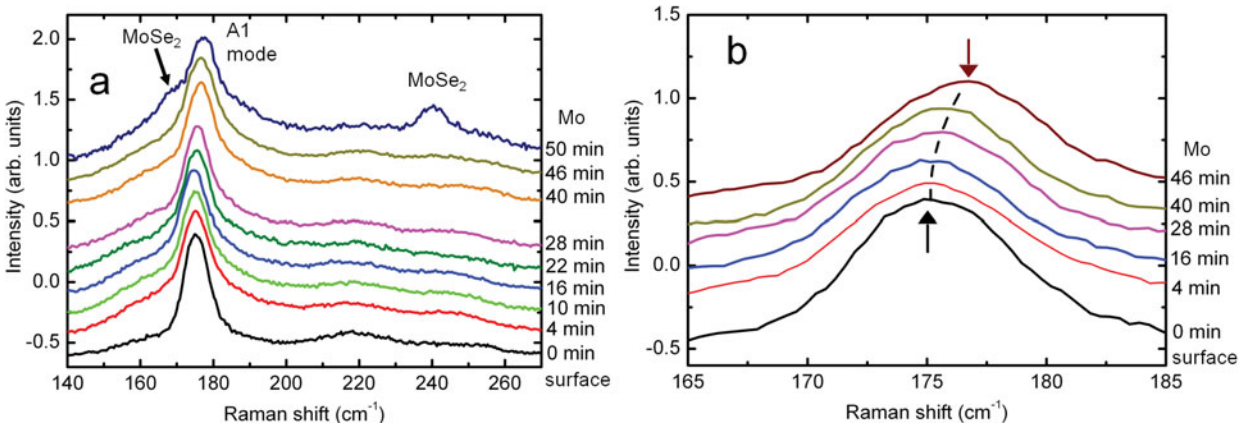

Figure 3. a: Raman spectra measured after sputtering the layer down to various depths (these spectra are shifted vertically). **b:** Enlarged section from panel **a**, between 165 and 185 cm^{-1}. Peak shifts of the A_1 mode with increasing sputtering depths are apparent (the maxima of the peaks are highlighted by ticks).

The discharge voltage applied was 650 V, the discharge current 6.5 mA, and the discharge gas flow 450 mL/min. Prior to analyzing the sample, the required isotopes to be detected for the elements of interest as well as the scan and integration durations for the selected isotopes were determined. Care was taken to achieve the maximum scan speed available (approximately seven scans per s). Each data point shown in the GD-MS data in Figure 2 represents an average of three scans.

The low current used was also favorable to avoid breaking the glass substrate due to local thermal stress from the glow discharge. As an additional measure, the Peltier cooling device of the instrument was switched to heating mode, so that the sample was kept at 40°C to achieve a smaller heat difference between sputtered area and the rest of the sample.

Data acquisition was started simultaneously with the glow discharge. The resulting profile indicated that the sample substrate was reached after 750 s. For each scan, the instrument yielded a semiquantitative concentration for the matrix elements analyzed.

The basic principle for evaluation in GD-MS is based on ion-beam ratios (IBR) and relative sensitivity factors (RSF). For each scan, the measured intensities for each isotope are normalized to the total ion beam measured. These IBR are multiplied with a sensitivity factor (RSF) to calculate concentrations. As is common practice in GD-MS, also unknown samples can be analyzed semiquantitatively by using a default set of RSF values. This standard RSFs table was determined for a steel matrix but can also be applied semiquantitatively to other sample compositions. Typical errors introduced are ±30 rel.%. As a consequence for time resolved analysis, each data point shown has been quantified based on the default sensitivity factors, according to the IBR measured at this point. Although absolute sensitivity may vary over the sputter time, according to the composition of the corresponding layers, the normalization to the total matrix current and subsequent proportional use of RSF values is a valuable approach for depth profile analyses.

Raman Depth Profiling

Raman scattering measurements were performed using a Horiba Jobin-Yvon T64000 spectrometer with an Ar^+ laser excitation source (514.5 nm) in backscattering configuration. The penetration depth of scattered light in $CuInSe_2$ is estimated to below 100 nm, assuming an absorption coefficient at the given wavelength of 10^5 cm^{-1} (Firoz Hasan et al., 1999). The focused spot size on the surface of the samples was about 100 μm, with an excitation power of 20 mW. In-depth resolved measurements were performed by acquiring sequentially a series of Raman spectra after sputtering the sample with the Ar^+ beam from a Phi 670 scanning Auger nanoprobe (Álvarez-García et al., 2001). To minimize damage in the sputtered region, the energy of the Ar^+ beam during ion sputtering was below 5 keV.

The sputter rate can be estimated taking into account that the time required to sputter the whole $Cu(In,Ga)Se_2$ layer is about 53 min. Assuming a thickness of about 1.8 μm (from the results obtained by EDX in transmission electron microscopy, see the Energy-Dispersive X-Ray Spectrometry in a Transmission Electron Microscope subsection below), the sputter rate results in about 34 nm/min.

Figure 3 shows the Raman spectra measured after sputtering the surface of the layer at different depths. All the spectra are normalized to the intensity of the main peak corresponding to the $Cu(In,Ga)Se_2$ A_1 mode, and the spectra measured after various sputter durations are vertically shifted. A contribution to these spectra at the 150–170 cm^{-1} region is visible, which is characteristic for the damage induced by the sputter process. This damaging also induces slight broadening of the peak. However, measurements performed in reference samples show not any influence of this process on the position of the main A_1 mode. The spectrum acquired after 50 min sputtering exhibits the presence of modes at about 169 and 240 cm^{-1} that are characteristic for the $MoSe_2$ layer present between Mo and $Cu(In,Ga)Se_2$.

Fitting of these spectra with a Lorentzian curve allows determination of the main A_1 peak of $Cu(In,Ga)Se_2$. This A_1 peak shifts toward higher frequencies with increasing

depth (Fig. 3b), which is directly related to the increase in the local Ga content in the $Cu(In,Ga)Se_2$ alloy toward the interface with the Mo back contact. Raman scattering measurements performed with the same experimental setup on reference $CuInSe_2$ and $CuGaSe_2$ layers give values for the frequency of the A_1 mode of 173 cm^{-1} ($CuInSe_2$) and 183 cm^{-1} ($CuGaSe_2$) (Rincón & Ramírez, 1992; Caballero et al., 2010). In the case of a $Cu(In,Ga)Se_2$ alloy, the position of the A_1 mode shows a linear dependence on the relative Ga content. It increases linearly with the [Ga]/([In] + [Ga]) ratio from the position corresponding to $CuInSe_2$ ([Ga]/([In] + [Ga]) = 0) to that characteristic of $CuGaSe_2$ ([Ga]/([In] + [Ga]) = 1) (Tanino et al., 1993). This allows for obtaining an estimation of the in-depth [Ga]/([In] + [Ga]) distribution, and therefore the distributions of [In] and [Ga] in the layers are determined assuming constant Cu and Se distributions and that [Cu] + [In] + [Ga] + [Se] = 1 in the layers.

In the interpretation of the present Raman spectroscopy data, we also assume that there are not any disorder or stress effects present in the Raman spectra affecting the frequency of the A_1 mode. Higher in-depth spatial resolutions (up to the order of 100 nm) can be achieved by decreasing the sputter duration between consecutive Raman scattering measurements because of the high light absorption in $Cu(In,Ga)Se_2$.

Nondestructive Techniques

Rutherford Backscattering Spectrometry

Helium-4 Rutherford backscattering spectrometry (RBS) measurements (Chu et al., 1978) were performed at the PSI/ETH EN tandem accelerator at beam energies of 2 and 5 MeV. Backscattered He ions were detected by a Si detector under an angle of 165°. The sample was tilted by 10° against normal incidence.

RBS with He has the advantage that elastic scattering cross sections and specific energy loss of these ions in materials are well known. As a consequence, the measured stoichiometries and the depth scale of concentration profiles are accurate to better than 5%. The main disadvantage is the insufficient mass resolution to separate Cu and Ga and the fact that the interpretation of the data is not unambiguous due to the superposition of all concentration depth profiles in one single spectrum. This ambiguity can be partly resolved by using different scattering or target tilt angles and different beam energies. A measurement at 2 MeV beam energy yields the composition at the very surface of the sample, though with very limited mass resolution. With a beam energy of 5 MeV, the He ions penetrate the whole layer, and the mass resolution is 2.5 times better than at 2 MeV. Since the depth scale in RBS is compressed with increasing beam energy, the depth resolution is worse at 5 MeV, though. Even at 5 MeV, the ambiguity of interpretation of the profile is not completely resolved.

To obtain the In in-depth distribution profiles, the stoichiometric numbers of Se and Cu have been set to 2 and 1. Then a number of six sublayers of various [Ga]/[In] ratios were fitted to the spectrum by the RUMP simulation software (Doolittle, 1986). By the total energy loss of He ions in the $Cu(In,Ga)Se_2$ layer, the thickness is estimated to be approximately 2.1 μm. Helium-4 energies higher than 5 MeV may not be used because scattering cross sections start to be "non-Rutherford," and nuclear resonances and reactions become possible.

To enhance the separation of Cu and Ga at the sample surface, heavy-ion backscattering has been performed with 15 MeV ^{28}Si projectiles. A high-resolution annular gas ionization detector was used to detect backscattered particles under an angle of 176°. These measurements confirmed the Ga/In ratio found by He-RBS at the layer surface (approximately 0.5 μm). In addition, the assumption about the Cu and Se concentrations was confirmed as well in this depth range. The resulting profiles determined by RBS and the other nondestructive techniques are shown in Figure 4.

Heavy Ion Elastic Recoil Detection

Heavy ion elastic recoil detection (HI-ERD or HI-ERDA) measurements (L'Ecuyer et al., 1976) were performed at the Munich Tandem accelerator using a ΔE-E_{res} detection system described in Bergmaier et al. (1998). ERD using swift heavy ions has the advantage that elastic scattering cross sections and specific energy loss of these ions in materials are well known. As a consequence, the measured stoichiometries and the depth scale of concentration profiles are as accurate as better than 5 rel.%. See Figure 5 for the raw data of the ERD measurements.

The technique is most suitable for the analysis of light and medium heavy elements ($1 \leq Z \leq \sim 30$, where Z is the atomic number) in thin layers. A depth resolution of about 10 nm can be achieved with common detection techniques due to the large stopping forces of the heavy ion beams. On the other hand, these large stopping forces also limit the measurable sample thickness, especially if an elemental discrimination of heavy target elements is required, as in the case of the $Cu(In,Ga)Se_2$ layer.

For the analysis of the $Cu(In,Ga)Se_2$ layer, an ion beam of 310 MeV ^{197}Au was prepared, which is the most heavy ion beam at maximum energy possible at the Munich accelerator. The incident angle of the beam ions was 20° with respect to the sample surface; the elastically scattered sample atoms were detected at an angle of 38°. From the energy spectra of the individual elements, quantitative depth profiles were calculated using the computer code KONZERD (Bergmaier et al., 1995).

Angle-Dependent Soft X-Ray Emission Spectroscopy

Angle-dependent X-ray emission spectroscopy (AXES) is a nondestructive, photon-in, photon-out technique that provides depth-dependent information on the elemental composition of a sample. It also yields the chemical environment of the probed atoms. However, this information is not used in the context of the present work. To obtain sufficient intensity and tunable excitation energy, synchrotron radia-

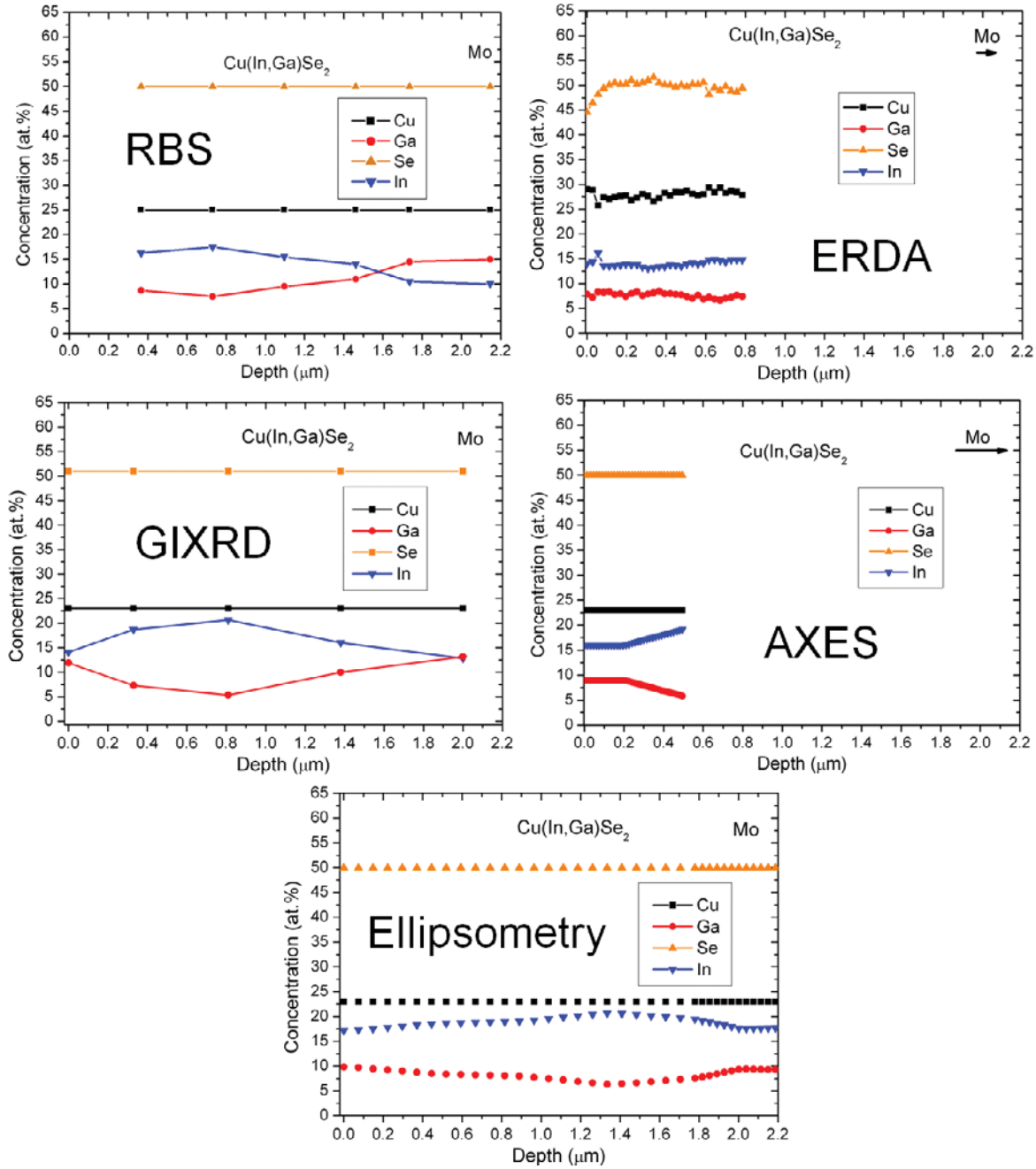

Figure 4. Elemental distributions acquired by means of "nondestructive" techniques.

tion is desirable as an excitation source. Thus, the experiments were conducted at the U 41 PGM beamline at the BESSY electron storage ring. The emitted radiation was analyzed using a Gammadata Scienta XES-300 soft X-ray grating spectrometer. The information depth ranges from a few tens up to hundreds of nanometers, depending on the relative sample tilt angle, the excitation and emission energies, as well as the absorption behavior of the sample. When changing the sample tilt angle and keeping all other factors constant, elemental-distribution depth profiles can be extracted from the integrated intensities of the emission peaks. In the used set-up, the angle between excitation and detection is fixed at 90°, while the exit angle β is used to control the information depth (see Fig. 6). A minimum information depth can be obtained at grazing incidence ($\beta \rightarrow 90°$) and grazing exit ($\beta \rightarrow 0°$) geometries, while between these extremes, a maximum of information depth is obtained. To achieve a higher accuracy and to minimize effects due to roughness, relative peak intensities are evaluated at a series of different exit angles β. This implies that the results monitor exclusively relative concentrations.

In our investigation of the depth-dependent elemental distributions of $Cu(In,Ga)Se_2$ thin films, we recorded Cu-$L_3M_{4,5}$, Ga-$L_3M_{4,5}$, and In-$M_{4,5}N_{2,3}$ emission peaks at various emission angles β and used relative intensities to calculate the [Cu]/([Ga] + [In]) ratios as a function of sample depth.

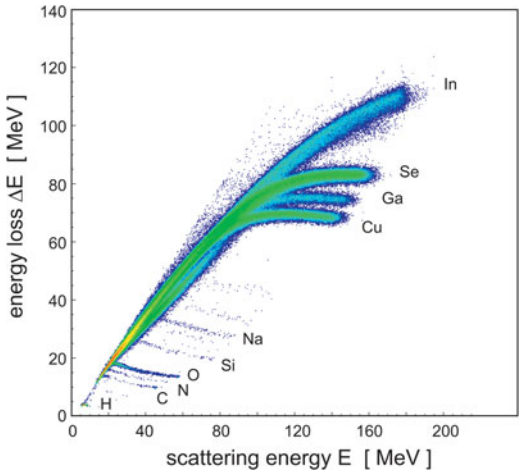

Figure 5. Raw data of the ERD measurement. The energy loss of the detected sample elements is plotted versus their scattering energy. Apart from the matrix elements (Cu, In, Ga, Se), various further impurities (H, C, N, O, Si, Na) were detected.

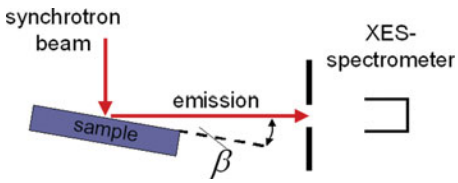

Figure 6. Elemental distributions acquired by means of "nondestructive" techniques.

To limit the extensive measurement time, we did not measure within an additional energy window covering the Se-$L_3M_{4,5}$ emission line. At excitation energies of 1,200 and 1,080 eV, a minimum information depth below 30 nm is obtained, while the maximum information depth is around 500 nm. With this, AXES covers a depth range that is difficult to probe by other nondestructive techniques.

To extract the depth profiles shown in Figure 4, we assumed the sum of the concentrations [Cu] + [Ga] + [In] + [Se] to be 1 (no Se emission was measured), and we assumed the ratio of cations to anions ([Cu] + [Ga] + [In])/[Se] to also be 1. A more detailed description of the technique and the modeling procedure is given in Mönig et al. (2008, 2010).

Grazing Incidence X-Ray Diffraction

The quantitative evaluation of grazing incidence X-ray diffraction (GI-XRD) is a nondestructive method for the analyses of in-depth elemental distribution profiles. The underlying idea is to calculate the shape of diffraction signals from a tentative set of compositional depth profiles and compare this simulated result with the measured data. The depth profiles are then modeled in an iterative procedure to fit the shape of the calculated reflections to the measured data (Kötschau & Schock, 2003, 2006).

Diffraction signals of Cu(In,Ga)Se_2 thin films with Ga/In compositional gradients generally show broadened, asymmetric peak shapes. This stems from the fact that the lattice plane distances—and therefore the 2θ position of a reflection—are influenced by these compositional gradients of this solid solution; i.e., in Cu(In,Ga)Se_2 thin films, the reflection position is a function of the layer depth. (Consequently, only those compositional variations affecting the lattice parameters considerably can be resolved.)

The actual depth information of the method stems from the attenuation of the radiation within the sample. The penetration depth of the radiation and consequently the shape of the diffraction signals depend on the incidence angle of the X-ray beam. By a variation of the incidence angle, the contribution of a diffraction signal from a certain depth is varied.

The GI-XRD patterns of the absorbers were collected on a *Panalytical X'Pert MPD Pro* system with Cu-Kα radiation ($\lambda = 1.54056$ Å) and a nickel Cu-Kβ filter. To focus the parallel beam, a 1/16° divergence slit and a 2 mm mask was used. The instrumental profile was defined by the measurement of a standard Si tablet, with the same configuration as used for the Cu(In,Ga)Se_2 thin film, at various incidence angles (0.5, 1.0, 1.5, 2.0, 2.5, 3.0, 4.0, and 5.0°) at 2θ ranging from 25 to 100°. Each of these Si patterns were refined by the Rietveld method, and single peak fits with a pseudo-Voigt function were applied to the 111 reflection. The position of the 111 reflection in the 2θ range is close to the 112 reflection of Cu(In,Ga)Se_2. Therefore, it was possible to determine the full-width at half-maximum accurately in this 2θ range, which is substantial for the extraction of compositional gradients by X-ray diffraction methods.

The presented calculation of the diffraction signals were performed by use of the simulation software TFXDAU. For a detailed description of this method, please refer to Kötschau and Schock (2006). The top layer of the sample was assumed to purely consist of Cu(In,Ga)Se_2 as confirmed by XRD measurements. The thickness of the Cu(In,Ga)Se_2 layer was set to 2 μm, according to the scanning electron microscope (SEM) image (see Fig. 1). For the simulation of the diffraction signals, the Cu(In,Ga)Se_2 layer was divided into 100 sublayers. For each sublayer, the Cu(In,Ga)Se_2 112 reflection peak was calculated from the assumed average composition of this sublayer using a pseudo-Voigt peak shape. The intensity of the peak from each sublayer was determined by the attenuation of the radiation due to mass absorption by the overlying sublayers depending on the incidence angle. Finally, the peaks of all sublayers are summed up to obtain the resulting total diffraction signal for a given incidence angle. The intensity of the total diffraction is additionally influenced by sample size and geometry of the setup. To rule out deviations between measured and calculated data stemming from these factors, the calculated diffraction signal intensities were scaled to agree with the signal intensities of the measured data.

For the data evaluation presented in this work, an automated fit routine was programmed to determine the parameters of the Ga depth profile. The number of these parameters was set to 5. Each parameter gives the atomic

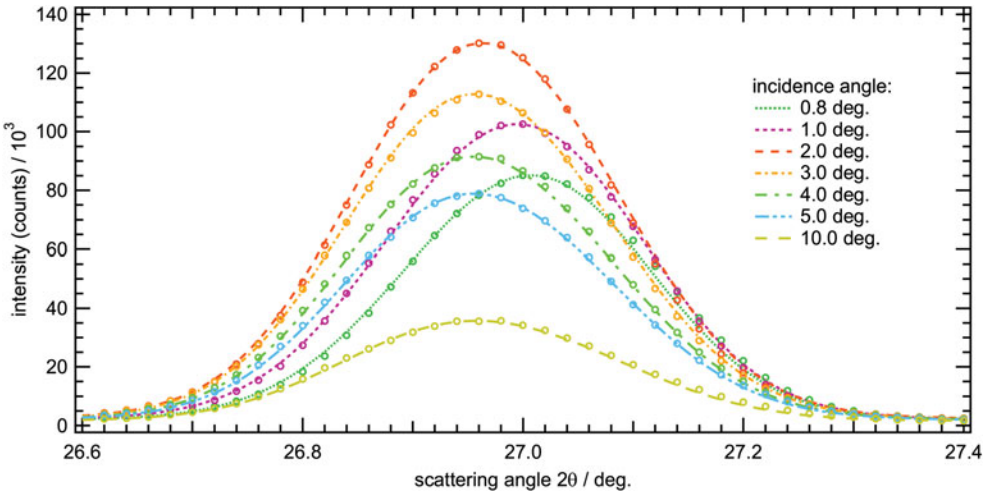

Figure 7. Measured (circles) and simulated (dashed lines) data for the Cu(In,Ga)Se_2 112 reflection for various incidence angles. The simulated diffraction peaks correspond to the Ga distribution shown in Figure 4 (GI-XRD data).

ratio [Ga]/([Ga] + [In]) for a certain point of layer depth *z*. The *z* values were held constant. The distance of the *z* values increases exponentially with the layer depth due to a decrease of sensitivity of the method with the depth. The complete course of the depth profile was determined by linear interpolation between the parameter points. The [Ga]/([Ga] + [In]) values for each parameter point were determined by a least-squares fit. The error square between simulated and measured diffraction data was minimized by a fit routine based on the Levenberg-Marquardt method (Levenberg, 1944; Marquardt, 1963).

Only the in-depth distribution of the ratio [Ga]/([Ga] + [In]) was modeled by the fit routine. The Se and the Cu depth profiles were set constant. The ratio [Cu]/([Ga] + [In]) was set to 0.88 according to the XRF measurements (Table 1). The ratio [Se]/([Cu] + [Ga] + [In]) was set to 1. The In in-depth distribution profile was calculated under the assumption that the concentrations of all matrix elements sum up to 100 at.%.

In Figure 7 the measured diffraction data for the Cu(In,Ga)Se_2 112 reflection for various incidence angles are shown together with the corresponding simulated data. The graph shows a good agreement between the measured and the calculated data.

A decrease of the ratio [Cu]/([In] + [Ga]) has a similar effect on the position of the 112 reflection as an increase of the ratio [Ga]/([In] + [Ga]). Therefore, by taking only the 112 reflection into account for the depth profile modeling, it is not possible to model both the Ga and the Cu depth profile. As a consequence, the Cu depth profile was set constant. If the Cu depth profile is changed, the Ga depth profile resulting from the least-squares fit would change as well. For example, if one assumed a decrease of the Cu content near to the surface of the sample, the simulation of the Ga profile would exhibit a lower Ga content near to the surface. This uncertainty can be solved by taking further reflections into account because changes in the Ga and Cu contents influence the Cu(In,Ga)Se_2 lattice constants in a different manner (Stephan et al., 2009). Other properties such as domain size, microstrain, and macrostrain may also influence the reflection shape. An investigation of the resolution limits and the extension of the method to multireflection modeling will be published elsewhere (R. Mainz, unpublished).

Ellipsometry

Over the past few decades, spectroscopic ellipsometry has emerged as a nondestructive, noninvasive optical technique for characterization of the structure and optical functions of thin film solar cell materials and devices (Boccara et al., 1993; Collins et al., 1998). Ellipsometry derives its name from the measurement of the output polarization ellipse that is generated after a beam of light with a known input polarization ellipse has interacted with a sample, most commonly in a specular reflection configuration.

The very rough surfaces of Cu(In,Ga)Se_2 thin films at the thicknesses (1–2 μm) used in high quality photovoltaic devices imply that reference dielectric function determination for uniform films of various Ga and In ratios can be particularly challenging due to the suppression of the specularly transmitted and reflected light waves via scattering from the thin-film surfaces (Marsillac et al., 2010). When the surface roughness layer is very thick, the light beam may not penetrate very deeply into the bulk layer, particularly for high photon energies. In addition, typical optical models for the surface roughness that work well in describing thin (<10 nm) layers are oversimplified for the thick (>30 nm) roughness layers. Rather than a single roughness layer described as an effective medium of 0.5/0.5 (bulk material/void), a multilayer designed to simulate a surface region with graded void volume fraction ranging from 1 at the surface to 0 at the interface to the bulk is likely to serve as a better approximation. Because the surface roughness increases in thickness during film growth, one method for avoiding this problem is to perform measurements during film growth and to limit the total thickness of the film to

less than 100 nm (Walker et al., 2009). Another method for modeling of films with significant surface roughness is to perform the measurements at multiple angles of incidence so that a larger number of free parameters can be obtained with greater confidence. Throughout the present study, three angles of incidence, 65°, 70°, and 75°, were used for reference dielectric function determination of uniform layers and for depth-profiling analysis of the compositionally-graded $Cu(In,Ga)Se_2$ layer.

Spectroscopic ellipsometry data were acquired using a commercially available variable angle spectroscopic ellipsometer (Johs et al., 2001) in the rotating-compensator configuration with multichannel detection (Lee et al., 1998). The photon energy range of the instrument is 0.75–6.50 eV. Pairs of (ψ, Δ) spectra were collected with an acquisition time of 10 min at each angle of incidence. Experimental data were first collected on uniform reference $Cu(In,Ga)Se_2$ films, each film having a different value of the [Ga]/[In] ratio, but a uniform composition as a function of depth into the thin film. These data were analyzed using software based on a least-squares regression algorithm. This software determines the bulk and surface roughness thicknesses as well as the bulk layer dielectric functions that generate ψ and Δ datasets serving as best fits to the experimental datasets. In this analysis, the dielectric function of the surface roughness layer was deduced from that of the bulk layer by applying the Bruggeman effective medium approximation (EMA) assuming a 0.5/0.5 volume fraction mixture of bulk material and void (Fujiwara et al., 2000). With this approach, the resulting dielectric functions can be further fit assuming a single analytical expression based on optical transitions between parabolic bands in the neighborhood of the band structure critical points (Collins & Ferlauto, 2005). The best fit parameters in the expression, including not only the band gaps but also amplitudes and broadening parameters, are plotted as a function of the known [Ga]/[In] ratio for the set of samples, and these plots are fit using polynomials. Thus, in the analysis of the graded layer, the [Ga]/[In] ratio can be used directly as a free parameter because it uniquely defines the dielectric function through the polynomial coefficients, which generate the required analytical expression.

With this database, the optical model for the film with the graded structure can be established. This model consists of three major layers including bulk molybdenum, which acts as the substrate; the absorber layer, which was divided into 36 sublayers; and a surface roughness layer, which was modeled as usual by a 0.5/0.50 volume fraction mixture of the underlying sublayer material and void. The dielectric function of each sublayer was linked to the alloy composition as described in the previous paragraph.

The analysis of the graded absorber layer was performed in two steps. In the first step, the near surface composition in six sublayers was determined from the high energy (>2 eV) region of data where the light has a limited penetration depth. (Taking $CuInSe_2$ as an example, the inverse absorption coefficient, or penetration depth, at 2 eV is given by $\alpha^{-1} = 140$ nm, and information can only be extracted from a depth of about $3\alpha^{-1}$, or about 400 nm for energies of 2 eV and greater.) In the second step, the composition of the top surface was fixed at that deduced from the high energy range. Then the low energy range of 0.75–2 eV, which includes light that penetrates throughout the entire absorber layer structure, is used to extract the composition of the underlying 30 sublayers.

The first analysis step allowed for the determination of the $Cu(In,Ga)Se_2$ surface roughness layer thickness of $d_s = 21.2 \pm 0.3$ nm, and the second analysis step provided the bulk layer thickness of $d_b = 2{,}224.8 \pm 0.5$ nm for the graded $Cu(In,Ga)Se_2$ absorber. Uncertainty in the analysis of the [Ga]/[In] ratio profile arises because a different reference set of samples fabricated at the University of Toledo was used to establish the relationship of the dielectric function to [Ga]/[In] ratio. As long as this reference set of samples is also of device quality, the assumption is likely to be a good one; however, the deduced optical parameters, most importantly the fundamental (or lowest energy) band gap parameter built into the analytical expression, are more basic results of the analysis and not dependent on such uncertainties. To establish the molar compositional profile from the [Ga]/[In] ratio profile for the graded layer, fixed copper and selenium contents of 23 and 51 at.% (see Table 1) were assumed throughout the depth. Hence, although the [Ga]/[In] ratio can be determined through the entire thickness of the film, no information is currently provided by spectroscopic ellipsometry on the content or on the profile of Cu and Se. Such information may be extracted in the future if a reference dataset is available with a dielectric function expression that includes parameters depending on both, the alloy ratio and the Cu content. Finally, it should be pointed out that *ex situ* depth profiling of this type by spectroscopic ellipsometry is a significant challenge. This challenge can be overcome more easily through the use of real time spectroscopic ellipsometry, which has been demonstrated to provide composition profiles with subnanometer resolution (Fujiwara et al., 1998; Podraza et al., 2008).

Techniques Performed on Cross Sections

Energy-Dispersive X-Ray Spectrometry in a Scanning Electron Microscope

Cu, In, Ga, and Se distribution profiles across the $Cu(In,Ga)Se_2$ layer were extracted from corresponding EDX maps (256 × 196 pixels) acquired by use of a Thermo Noran X-ray detector and the Thermo Fisher Scientific software Noran System Six in a LEO GEMINI 1530 SEM, which is equipped with a field-emission gun. It has been shown (Barkshire et al., 2000) that spatial resolutions of down to 100 nm and below may be obtained in SEM-EDX measurements by reducing the acceleration voltage down to few kV. One prerequisite is that the acceleration voltage still is sufficient to excite the signals of all elements of interest in a sample, where in the present case, it is the In-L line, which exhibits the highest energy of the L lines of all matrix

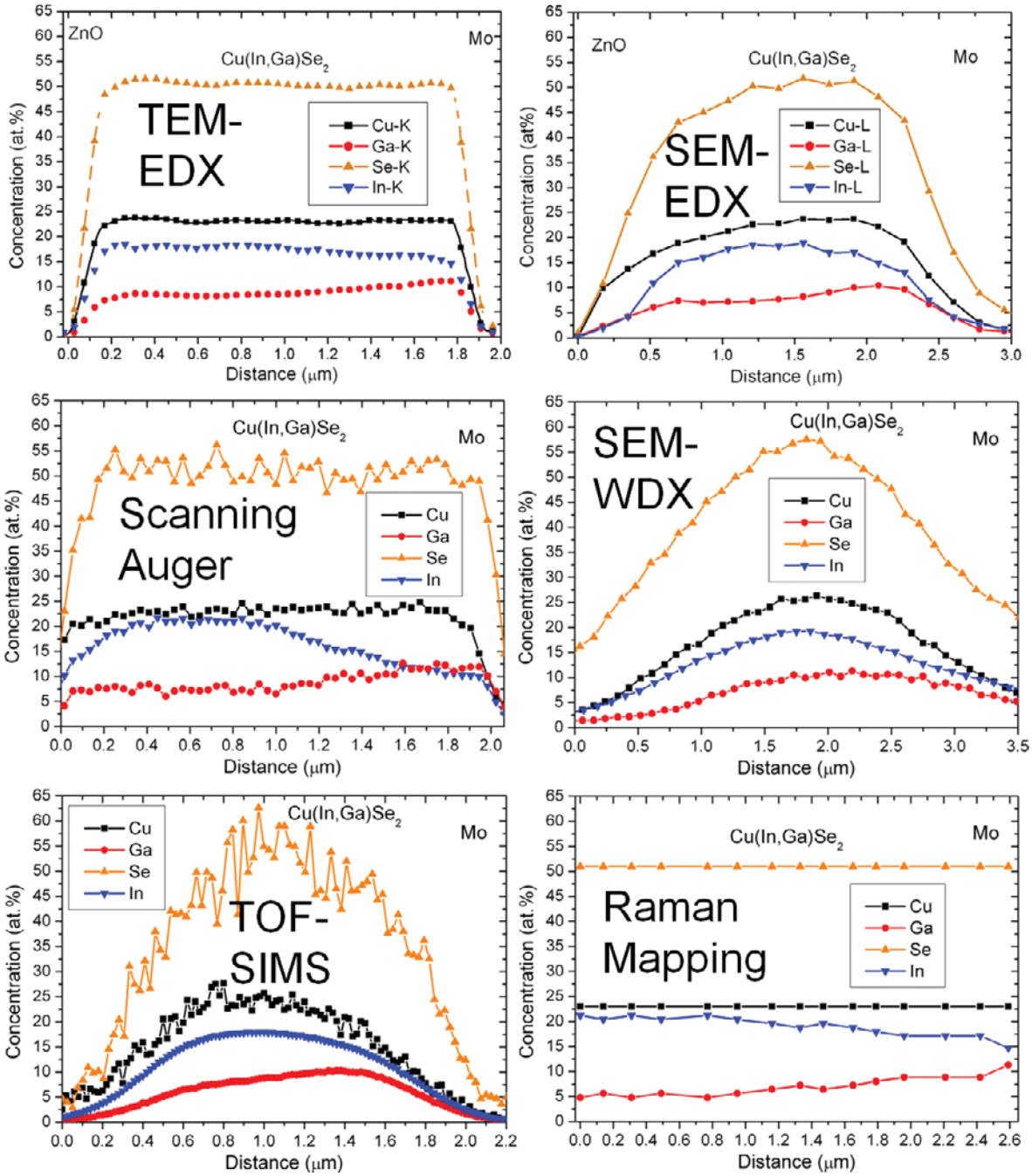

Figure 8. Elemental distributions acquired by means of cross-section techniques.

elements, of about 3.4 keV. To achieve a considerably high intensity of the In-L line, the acceleration voltage was set to 7 kV (beam current about 6 nA). A second prerequisite is that the EDX evaluation software is able to deconvolute efficiently Cu-L and Ga-L signals, which is presently the case for software packages provided by various manufacturers.

The given signals in Figure 8 are net counts, i.e., the background was subtracted, and the peaks were fitted and deconvoluted. The SEM-EDX signals were quantified by calculating average net intensity values for each of these across the $Cu(In,Ga)Se_2$ layer and relating these averages to the integral compositions determined by XRF (Table 1).

It is shown by the SEM-EDX data in Figure 8 that the local maxima in the Ga distribution profile located close to the Mo layer and near to the surface (or to the CdS/ZnO layers) are revealed, similarly as for the transmission electron microscope (TEM)-EDX (Fig. 8) and the XPS (Fig. 4) results. Thus, although the spatial (and depth) resolution is substantially worse for SEM-EDX compared with various other techniques, this method is able to measure elemental distributions of thin films with thicknesses of down to 30 nm (see, e.g., Abou-Ras et al., 2011). Naturally, the X-ray signals from very thin layers are broadened owing to the generation profile of the incident electron beam at (for

example) 7 keV. It is noteworthy that SEM-EDX may also be performed on fractured cross sections, e.g., if thin films are deposited on glass substrates (Kaufmann et al., 2009).

Wavelength-Dispersive X-Ray Spectrometry in a Scanning Electron Microscope

The Thermo Fisher Scientific parallel beam spectrometer MagnaRay was used to perform net count line scans of the elements Cu, In, Ga, and Se. The acceleration voltage was set to 20 kV, which enabled a free choice of lines over the energy detection range up to 12 keV with a standard equipment of four flat crystals (NiC80, TAP, PET, LiF). The MagnaRay spectrometer uses a patented hybrid X-ray focusing optic incorporating both a capillary and grazing incidence optic combined with a low-energy capable sealed xenon proportional counter for achieving high throughput. The adjustment of the atomic number Z is facilitated by use of an automated direct drive at an angular precision better than 10^{-3}°.

Fifty single spectra were acquired during the line scan for each element. The dwell time for each point was set to 5 s. The LiF diffractor was chosen for the analysis of Cu-K, Ga-K, and Se-K. In-L was measured using a PET diffractor. The given signals in Figure 8 are net counts, i.e., the background was subtracted, and the peaks were fitted and deconvoluted. Similarly as for SEM-EDX, the SEM–wavelength dispersive X-ray (WDX) signals were quantified by calculating average net intensity values for each of these across the $Cu(In,Ga)Se_2$ layer and relating these averages to the integral compositions determined by XRF (Table 1).

The WDX measurements reveal the same trend as the EDX measurements. It can therefore be assumed that statistically reliable results are obtained in a few minutes for each element.

One main advantage of WDX spectrometers lies in the ability to detect approximately one power of ten smaller amounts of trace elements, compared with EDX. The concentration ranges of the $Cu(In,Ga)Se_2$ solar cell are in an order of magnitude that also allows good-quality EDX measurements.

Another major advantage of WDX compared with EDX is better energy resolution. This is often very important for the correct identification of element lines that cannot be separated by EDX.

Energy-Dispersive X-Ray Spectrometry in a Transmission Electron Microscope

Elemental distribution profiles of Cu-K, Ga-K, Se-K, and In-L signals were acquired across the $Cu(In,Ga)Se_2$ layer by use of the Thermo Fisher Scientific Noran System Six acquisition software and a liquid N_2-cooled Thermo Noran X-ray detector at a Zeiss LIBRA 200 FE TEM. It is the advantage of TEM-EDX as compared with SEM-EDX that the TEM lamella prepared for the present study was quite thin (about 30–50 nm at the position of analysis), i.e., the excitation volume was quite small and thus the achievable spatial resolution high, about 2 nm. We estimate, however, the actual spatial resolution slightly larger to about 5 nm, as estimated from the decrease of signals at the interfaces to CdS/ZnO and to Mo.

The acceleration voltage applied was 200 kV, the point-to-point distance 20 nm, the total number of points 100, and the dwell time 5 s. The signals given in Figure 8 are net counts, i.e., the background was subtracted, and the peaks were fitted and deconvoluted. Similarly as for SEM-EDX, the TEM-EDX signals were quantified by calculating average net intensity values for each of these across the $Cu(In,Ga)Se_2$ layer and relating these averages to the integral compositions determined by XRF (Table 1).

While the analysis of elemental distribution in about 2 μm thick layers is not difficult to perform by means of TEM-EDX, it is challenging to study interdiffusion at the nanometer scale between the various layers in the solar-cell stack (e.g., Abou-Ras et al., 2005) or also elemental distributions within individual layers (e.g., Platzer-Björkman et al., 2006). Presently, spatial resolutions in TEM-EDX measurements as high as 0.4–0.6 nm may be achieved by use of aberration-corrected microscopes (Watanabe et al., 2006).

Scanning Auger Electron Microscopy

The test specimen is excited by bombardment with electrons to emit Auger electrons. These electrons refer to the uppermost approximately 5 nm of the surface and are detected by use of an electron spectrometer consisting of an energy analyzer and an electron detector system. The measured energies of the Auger electrons can be correlated to corresponding elements.

A PHI 700 scanning Auger spectrometer manufactured by Ulvac-PHI, Inc. (Kanagawa, Japan) was used for the present analysis. The Auger electron emission was excited by a primary electron beam of 10 kV at 1 nA. The size of the analyzed area on the sample was about 5 μm × 5 μm. Surface contaminations that suppress Auger signal intensities were removed by 22 s sputtering with 3 keV Ar^+-ions on an area of 0.8 mm × 0.8 mm at a beam current of 2 μA. To compensate for charging effects, the sample was tilted to 60° with respect to the surface normal and flooded by 70–90 eV Ar^+ ions. By applying these conditions, line scans of Ga, Se, Cu, In, Zn, O, Mo, Si, and S were acquired on the cross-sectional sample of the $ZnO/CdS/Cu(In,Ga)Se_2/Mo/$glass solar-cell stack. Quantification was performed by relating the averages of the signal intensity distributions to the integral concentrations given in Table 1.

Time-of-Flight Secondary-Ion Mass Spectrometry

Time-of-flight secondary-ion mass spectrometry (TOF-SIMS) is applied for qualitative determination of atomic and molecular composition of the top surface layers. The sample surface is bombarded by a primary ion beam (Ga^+, Au^+, In^+, Bi^+, Cs^+, oxygen, or noble gas ions), which creates an atomistic collision cascade into the bulk. Due to energetic transfer the atomic lattice of the near surface region (one to two atomic layers) is destroyed, and atoms as well as molecular fractions leave the surface. Most of emitted parti-

cles are neutrals, but some are positively or negatively charged. The mass analysis of positive (SIMS+) and negative (SIMS−) charged particles are carried out by a TOF mass spectrometer.

A TOF-SIMS IV system manufactured by ION-TOF Ltd. Münster (Germany) was used for the present analysis. 25 keV $^{69}Ga^+$ ions were applied. Elemental distribution maps were acquired by scanning the primary ion beam on an area of 4 μm × 4 μm across the cross-sectional sample of the ZnO/CdS/Cu(In,Ga)Se_2/Mo/glass solar-cell stack. Charging of the electrically nonconducting sample was compensated by low energy (18 eV) electron flooding of the analyzed surface area. Signals of Al, Cu, ^{71}Ga, In, Mo, O, Se, Si, and Zn (SIMS+) as well as O, S, Se, Si, AlO_2, CSO, Cu_2O_2, GaO, and MoO_3 (SIMS−) were detected (note that the Ga isotopes for the primary beam and for the TOF-SIMS signals are different, i.e., possible Ga implantations do not affect the measurement results). The line scans given in Figure 8 (TOF-SIMS) are averages from several individual line scans extracted from elemental distribution maps. Quantification was performed by relating the averages of the signal intensity distributions to the integral concentrations given in Table 1.

Raman Mapping

A cross-sectional sample of the ZnO/CdS/Cu(In,Ga)Se_2/Mo/glass solar-cell stack was investigated using a combined atomic force microscopy (AFM) and Raman 'NTegra Spectra' system (NT-MDT, Zelenograd/Moscow, Russia). The upright microscope system is equipped with a 100×/ N.A. = 0.7 long-working distance objective with an AFM module mounted between objective and sample. Design of the objective and shape of AFM cantilevers ("nose-type" ATEC cantilevers, Nanosensors, Neuchatel, Switzerland) allow simultaneous AFM and optical measurements on the exactly same part of transparent and opaque samples. The system is equipped with a white-light microscope module and with a video camera for observation and rough alignment of the sample, a confocal scanning microscope module with photomultiplier tube detector for laser-based imaging, and a spectrometer with four different interchangeable gratings and CCD detector (Newton, Andor, Belfast, Northern Ireland, UK) for Raman measurements. The system is controlled by the NT-MDT Nova software, which allows simultaneous AFM imaging and Raman mapping experiments. All measurements for the present study were performed using a 632.8 nm HeNe laser, which was attenuated to a power of approximately 0.5 mW at the sample using neutral density filters in the NTegra Spectra system. This laser power did not lead to detectable sample damage or change of Raman spectra, which has been verified by applying measurement durations 2–120 times longer than for the Raman results shown in the present work. No changes in band positions or relative intensities were found.

AFM imaging and Raman mapping were performed on the identical part of a cross-sectional ZnO/CdS/Cu(In,Ga)Se_2/Mo/glass sample in semicontact mode ("tapping mode"). By scanning the sample through the laser focus and collecting the whole Raman spectrum at each pixel, a Raman signal-distribution map was acquired. The collection duration per spectrum (pixel) was 5 s, resulting in a total measurement duration of 5.7 h for a 64 × 64 pixel mapping. The AFM image was recorded with a higher resolution of 256 × 256 pixels. The optical resolution of our system has previously been demonstrated to be approximately 400 nm (Schmid et al., 2009). During the Raman mapping experiment, the AFM was engaged for two reasons: check for possible sample drifts and movement of the sample in z direction according to its topography as "auto focus" for the optical measurements.

A line scan with high spatial and high spectral resolution was acquired on the cross-sectional sample. Instead of the 600-line standard grating (approximately 1.2 cm^{-1} spectral resolution), an 1,800-line grating with a resolution of approximately 0.4 cm^{-1} was applied. This was necessary to detect small band shifts close to the Cu(In,Ga)Se_2/Mo interfaces. The gain in spectral resolution was accompanied by an approximately ten times smaller signal intensity and a three times smaller spectral range. The latter was not a limiting factor in this study. A line scan of 10 μm across the sample was performed with a lateral resolution of 128 pixels or approximately 80 nm per pixel. The collection time per pixel was 300 s, leading to a total measurement time per line of more than 10 h.

Figure 9 shows selected Raman spectra collected during the line scan. The spectra were background corrected, and the intensities of the most prominent bands at 175 cm^{-1} (Witte et al., 2009*a*) were normalized to 1 for better comparability. Also, the spectra were stacked by introducing offsets of 0.2. For the Cu(In,Ga)Se_2 band at 175 cm^{-1}, small band shifts can be detected close to the interface to the Mo layer. Also, an additional band at 240 cm^{-1} appears close to the edge, which can be assigned to $MoSe_2$.

Information on the stoichiometry of Cu(In,Ga)Se_2 can be derived from the Raman shifts or exact band positions (see also the Raman Depth Profiling subsection above). The raw data show steps corresponding to the spectral resolution of approximately 0.4 cm^{-1}. Smoothed data were obtained by fitting a Lorentz-type function to each A_1 band and plotting its position versus distance (see Fig. 8). Band shifts of up to 2.5 cm^{-1} are detected at distances of approximately 1 μm from the Mo layer, related to the increasing Ga content toward the interface with the Mo back contact. The In and Ga in-depth distribution profiles can be derived taking into account the linear dependence of the frequency of the A_1 mode on the [Ga]/([In] + [Ga]) ratio, similar to the procedure described in the Raman Depth Profiling subsection above.

Comparison of the Ga Distributions Obtained by the Various Techniques

To compare the Ga distribution profiles obtained by the methods presented in the previous section, they are shown in Figure 10. To provide comparability between all these

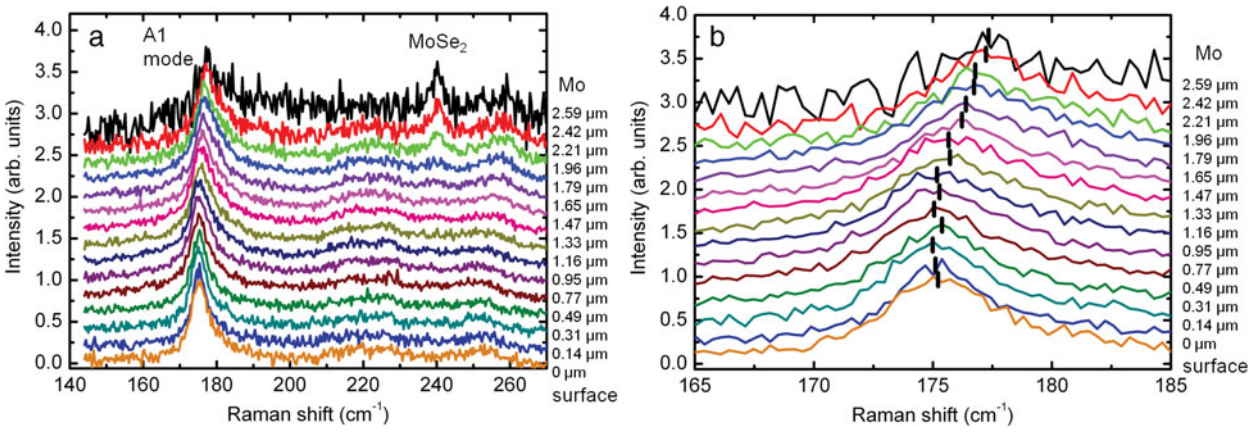

Figure 9. **a:** Raman spectra collected in a line scan across the $Cu(In,Ga)Se_2$ layer in a solar-cell stack. Only each second spectrum of all acquired is shown. The lateral distances are given on the right side of the spectra. A $MoSe_2$ band close to the interface to the Mo layer is visible. **b:** Enlarged section of panel **a**, between 165 and 185 cm^{-1}. Note the shift of the A_1 band, indicating increased Ga concentrations when moving from the surface (0 μm) to the Mo layer (2.59 μm).

results, the spatial scales were adjusted such that the $Cu(In,Ga)Se_2$ layer thickness was 2 μm. Most of these profiles feature a larger Ga concentration close to the Mo back contact than close to the surface (or to the CdS/ZnO layers). While ERDA and AXES were able to provide elemental distributions only down to depths of 800 and 500 nm, the ellipsometry result shows a slightly higher Ga concentration close to the surface of the $Cu(In,Ga)Se_2$ layer than close to the Mo layer. XPS, GD-OES, GD-MS, TEM-EDX, and SEM-EDX exhibit clearly the presence of a local maximum in the Ga distribution close to the surface, which is also indicated ambiguously by the RBS, the GI-XRD, the AXES, and the ellipsometry results.

It is definitely challenging for the application of the techniques that the Ga concentration varies only slightly on a length of about 2 μm, between about 7 at.% close to the surface and about 12 at.% close to the Mo layer, with a local minimum of about 6 at.% (taking the XPS result as reference). For thin films with substantially larger compositional variations on similar length scales, several of the techniques compared in the present work, e.g., SNMS, have shown better performances (e.g., Hodoroaba et al., 2001). It should also be mentioned that ERDA and AXES are very useful techniques especially for very thin films of few hundreds of nanometers, which are outperformed by several other techniques when applied on the total thickness of few micrometers thick layers.

Discussion

An important question for us to answer was which technique is best to measure elemental distributions in thin films. We conclude that, after evaluating the data obtained by the various techniques, we were not able to identify any method that would be able to determine satisfactorily the quantitative elemental distributions across a layer with unknown composition. For precise quantitative elemental distribution analysis with accuracy of 1 at.% and below, it is necessary to consult yet another technique for verification of elemental distributions or for quantification of the acquired data.

For the elemental distributions obtained by most of the techniques, the average signal intensity distributions were calibrated by means of the XRF measurement (Table 1); such a calibration was not necessary for Raman depth profiling and mapping, as well as for RBS, ERDA, GI-XRD, AXES, and ellipsometry. This indicates that one approach of a quantitative elemental distribution analysis may be to acquire the net-count intensity distribution and use an integral quantitative measurement as a reference. Also for measuring the qualitative distributions, it is helpful to employ more than only one technique because such an individual result often remains ambiguous, with uncertainties concerning measurement artifacts and limitations impeding a high quality of the resulting elemental distributions.

All measurement techniques that were presented above have their advantages and disadvantages, and it is the specific requirements of the elemental distribution analysis that determine which method to choose. A first general remark concerns the analysis geometry. Depth-profiling techniques and those that are termed "nondestructive" in the present work, both analyzing the thin film from the top, do not require any sample preparation and give (in part) information on elemental distributions in short time. However, if thin films exhibit substantial compositional variations in their lateral extensions, it may be more favorable to look at cross-sectional samples.

Several of the techniques presented in this work use ion sputtering generating craters in the thin film. Roughness at the borders of the craters affect the measurement results substantially, and the sputter yield also may change for varying in-depth phase compositions. Thus, it is necessary to adjust for these effects by, e.g., rotating or cooling the sample as well as by post-processing the data. Often, sputter conditions need to be adjusted specifically for a material system under investigation.

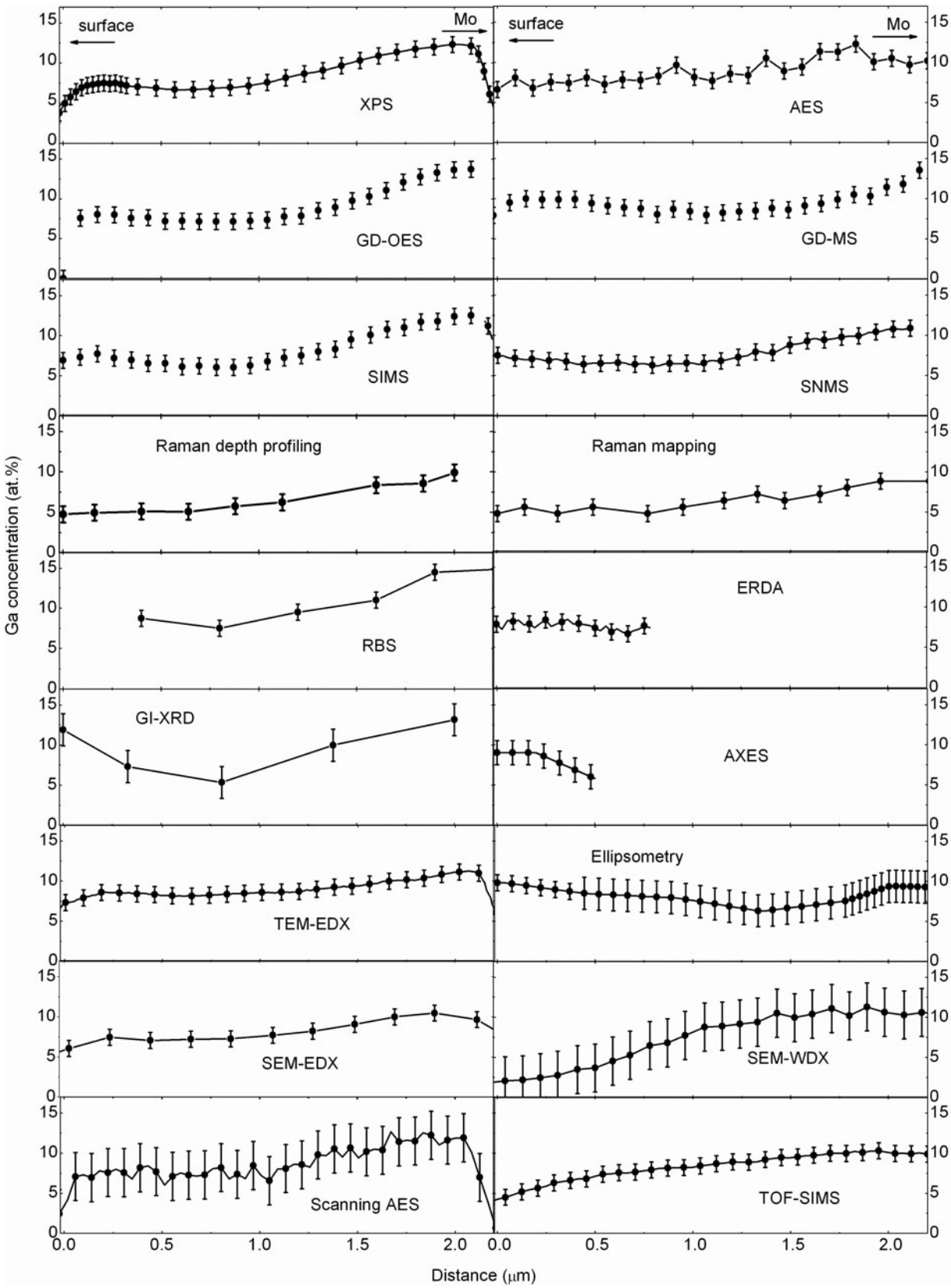

Figure 10. Ga distributions across $Cu(In,Ga)Se_2$ obtained by various techniques. The surface is positioned left from 0 μm, the Mo layer right from 2.2 μm. The lines in the graphs are guides for the eye. The error bars are estimates individually for each technique. Note that these error bars do not overlap for all techniques and for all positions; i.e., it can generally not be stated that the "real" concentration values are to be found within the intervals given by the error bars.

Table 2. Techniques Applied for the Analysis of Elemental Distributions in Thin Films and Their Characteristics.*

Technique	Analysis Mode	Lateral Resolution (nm)	Depth Resolution (nm)	Duration (min)	Availability	Detection Limits (at.%)	Quantification of Results
SIMS	DP	5×10^3	4	45	Good	10^{-7}–10^{-3}	Standard
SNMS	DP	10^6	1	120	Medium	0.05	Standard
GD-OES	DP	10^6	3–100	5	Good	10^{-5}–10^{-3}	Standard
GD-MS	DP	10^7	10	10	Medium	10^{-7}–10^{-5}	Standard
AES	DP	10^5	10	45	Good	0.3	Standard
XPS	DP	10^5	1–10	120	Good	0.1	Standard-free
Raman depth-profiling	DP	10^5	100	50	Medium	1	Standard
RBS	Surf	10^7	10	10	Rare	1	Standard-free
ERDA	Surf	10^7	10	30	Rare	10^{-4}	Standard-free
GIXRD	Surf	10^6	100	420	Good	1	Difficult
AXES	Surf	10^5	10–80	420	Rare	1	Standard
Ellipsometry	Surf	10^6	1	30	Medium	0.2–2	Difficult
TEM-EDX	CS	5	Specimen thickness	30	Good-medium	0.5	Standard
SEM-EDX	CS	150	Few 100	20	Good	0.5	Standard
SEM-WDX	CS	150	Few 100	60	Good	3	Standard
Scanning Auger	CS	10	1	137	Good	3	Standard
TOF-SIMS	CS	100	1	2	Medium	10^{-6}	Standard
Raman mapping	CS	400	100	120	Medium	1	Standard

*DP, depth profiling (destructive); Surf, analysis from the surface (nondestructive); CS, analysis on cross section. Note that all given values correspond to the measurement conditions used for the present work; they may differ substantially for other analysis parameters applied. The lateral resolutions refer to the minimum areas of acquisition for the DP and Surf techniques, and for the CS analyses to the minimum distance between two features still to be distinguished. The availability is divided into techniques frequently (good), in fewer numbers (medium), and rarely (rare) present in research labs. Accuracy of quantitative results refers to whether a technique needs calibration by reference samples or reference measurements (standard), which may be *difficult* in some cases (i.e., since the fitting of the model to the experimental data requires a large number of parameters), or whether a technique is entirely standardless. In any case, the accuracy of the determined atomic concentration of a matrix element within an elemental distribution profile (in contrast to an integral compositional measurement) is hardly smaller than 1 at.%.

In the following, all methods are discussed with respect to their strengths. The idea is to identify requirements for which a method is particularly suitable (see Table 2):

- When aiming for fast acquisitions with the possibility of also measuring the distributions of trace elements, GD-OES and GD-MS may be the techniques of choice, which need only about 5–10 min to analyze a 2 μm thick $Cu(In,Ga)Se_2$ layer.
- High depth resolutions may be achieved by means of AES, XPS, AXES, ellipsometry, (TOF)SIMS, and SNMS. SIMS is more sensitive to trace elements, whereas SNMS exhibits its strengths in probing the distributions of matrix elements.
- SIMS and TOF-SIMS, moreover, are techniques for analyzing small differences in the mass of the detected particles, which are even able to resolve isotopes of the individual elements.
- High sensitivities for trace elements are provided by ERDA and SIMS. ERDA is especially useful when studying light elements in a thin film of few nanometers up to a few hundreds of nanometers containing heavy matrix elements, while RBS is of particular advantage for the analysis of heavy elements in a light matrix.
- GI-XRD, AXES, and ellipsometry are nondestructive techniques. However, heating of and therefore phase transformations within the sample cannot be excluded, especially not when using high-intensity X-ray and light sources. Furthermore, the modeling of the experimental data is not unambiguous, as the probe signal of these nondestructive techniques is a convolution of signals from different depth layers. The deconvolution of these signals requires certain assumptions, which eventually lead to the extracted depth profiles. Also, the surface roughness of the thin film complicates the evaluation of the data.
- RBS and ERDA are not truly nondestructive because they do not generate craters in the thin film but substantially damage the sample surface. Also, it has to be considered that, for these two techniques, the ion beam particles are implanted deep into the material analyzed.
- High spatial resolution is provided by TEM-EDX and scanning Auger spectroscopy. It is substantially lower for SEM-EDX and SEM-WDX, but for these methods, the sample preparation is not as extensive and these methods also can be applied on fractured cross sections.
- Raman spectroscopy gives information not only on elemental distributions in-depth and laterally but also is able to identify secondary phases as well as the presence of point or extended defects inducing disorder, indicated by the shape of the Raman peaks.

Further Techniques Not Included in the Comparison

In this section, we would like to list a number of techniques that were not applied successfully for the elemental distribution analysis of the $Cu(In,Ga)Se_2$ thin films but that are established or promising methods for similar tasks.

Atom Probe Tomography

Atom-probe tomography (APT) has been traditionally applied in the field of physical metallurgy to the characterization of alloys but has recently become of great interest for the analysis of semiconductor materials and devices. Using this tool, it is possible to map the elemental distribution in three dimensions with subnanometer resolution (Kelly & Miller, 2007). Figure 11 schematically shows the principles of APT. By applying either high voltage or laser pulses to a positively biased tip-shaped specimen (having a radius of curvature $\leq$100 nm), surface atoms are successively ionized and field-evaporated. The field-evaporated ions are accelerated toward a position sensitive detector that records their TOF and impact positions. A three-dimensional (3D) elemental map is reconstructed from the collected data using an inverse point projection algorithm.

State-of-the-art atom probes with high-speed detector systems provide fast data acquisition rates (up to 10^6 ions/min) and a large field of view (up to 200 nm) (Miller, 2000; Gault et al., 2006; Kelly & Miller, 2007). Volumes containing up to several hundred millions of atoms can be probed within a few hours, and impurity concentrations as low as few tens of ppm can be traced. Modern instruments include ultrafast lasers (with pulse lengths ranging from about 10^{-13} to 10^{-11} s), thus enabling the analysis of semiconductors (Gault et al., 2006; Kelly & Miller, 2007). As a result, pulsed-laser APT has become of great interest for measuring local concentrations in $Cu(In,Ga)Se_2$ solar cells. First APT results on the distribution of Na in $Cu(In,Ga)Se_2$ layers grown with a NaF precursor on p-doped Si (Cadel et al., 2010) and on the distribution of Na and Fe impurities in completed solar cells on steel substrates (Schlesinger et al., 2010) have recently been published.

Typically, tip-shaped specimens are prepared by focused ion beam machines, using Ga ions and annular milling. To reduce the Ga implantation into the specimen, acceleration voltages and currents for the Ga ion beams have to be adjusted. For appropriate parameters (Thompson et al., 2007), the implanted zones exhibit widths of only a few nanometers. Since monoisotopic Ga is used, this zone can be identified easily and is disregarded in the data evaluation.

Grazing-Incidence X-Ray Fluorescence Analysis

In this new methodological approach, grazing-incidence X-ray fluorescence (GI-XRF) analysis is combined with calibrated instrumentation of the Physikalisch-Technische Bundesanstalt at the electron-storage ring BESSY II. Employing monochromatic synchrotron radiation with photon energies in the few keV range under grazing incidence conditions, a nondestructive access to the compositional depth profile of thin $Cu(In,Ga)Se_2$ films is provided because the information depth in GI-XRF can be scaled by the penetration depth tuneable by the incident angle or photon energy of the exciting radiation. The detection of fluorescence photons in combination with radiometrically calibrated instrumentation, including photodiodes, diaphragms, and energy-dispersive detectors, allows for a completely reference-free quantitative analysis, which does not require any standard samples for calibration purposes (Beckhoff, 2008). The quantification algorithm is based on calculations with atomic fundamental parameters, such as absorption cross sections, transition probabilities, and fluorescence yields, where the elemental depth gradients are approximated by a layer stack with an appropriate number of single-phase thin layers. Then, the calculated fluorescence line intensities can be iteratively adjusted to the absolute count rates obtained by reference-free measurements. The general suitability of the method for determining depth gradients in $Cu(In,Ga)Se_2$ thin films was already demonstrated by both, calculations and reference-free XRF investigations (Streeck et al., 2010).

Electron Backscatter Diffraction

Since the lattice constant ratio c/a of the tetragonal crystal structure of $Cu(In,Ga)Se_2$ is proportional to the Ga concentration (Suri et al., 1989), the distribution of this ratio across a polycrystalline thin film may be obtained by acquiring EBSD patterns on various points of a line scan within an individual grain (perpendicular to the interfaces in the ZnO/CdS/$Cu(In,Ga)Se_2$/Mo/glass stack) being contiguous from the top to the bottom of the layer (see Fig. 12 for an EBSD pattern-quality map and an exemplary EBSD pattern). EBSD is not able to deliver the absolute values for the lattice constants a and c but represents a sensitive tool for variations of these values.

From a given set of EBSD patterns acquired on a line scan across a $Cu(In,Ga)Se_2$ thin film, the variations in lattice constants c and a may be accessed by comparing selected diffraction bands in these experimental patterns with those in EBSD patterns simulated at known reference states (Zaefferer, 2002; Kacher et al., 2009). Alternatively, small shifts in features from one pattern to the next using cross-correlation functions may be evaluated (Wilkinson et al., 2006*a*, 2006*b*). However, apart from variations in the Ga concentrations, elastic strains also may cause changes in the lattice constant ratio c/a. Without the knowledge of the elemental distributions provided by another technique, it is not possible to separate the effects of compositional changes and strain, which is also why the EBSD technique was not further considered in the present comparison.

Cathodoluminescence

A cross-sectional sample prepared from a ZnO/CdS/$Cu(In,Ga)Se_2$/Mo/glass stack was analyzed by means of spatially resolved cathodoluminescence (CL) microscopy at low temperatures. The CL setup is based on a fully computer-

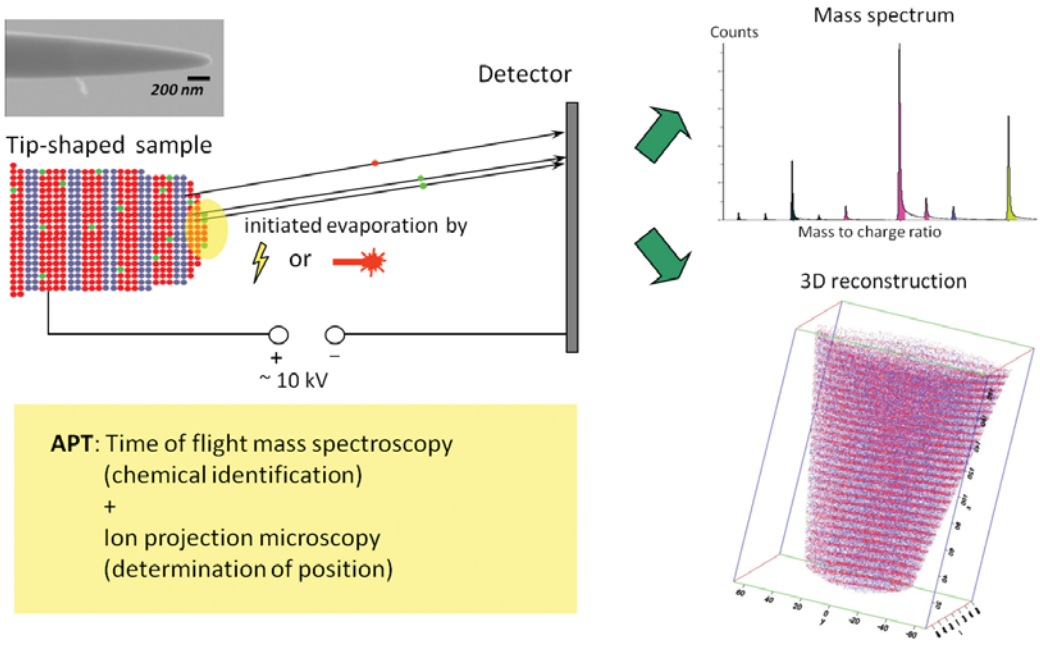

Figure 11. Principles of APT. A high voltage is applied between the tip of the sample and the detector. Mass spectra are acquired, and a 3D elemental map is reconstructed from the collected data.

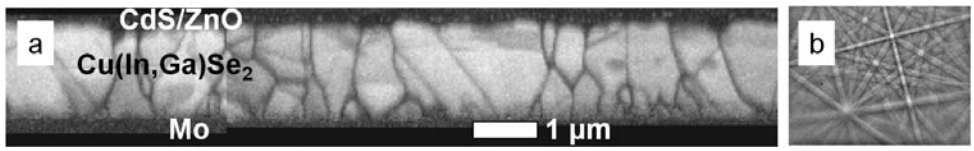

Figure 12. **a:** EBSD pattern quality map of the ZnO/CdS/Cu(In,Ga)Se_2/Mo/glass stack analyzed by various techniques for the present work. **b:** An individual EBSD pattern from a line scan acquired across a Cu(In,Ga)Se_2 grain being contiguous from the top to the bottom of the Cu(In,Ga)Se_2 thin film.

controlled modified SEM and provides an overall spatial resolution better than 25 nm under optimum conditions. In CL imaging mode, the focused electron beam is scanned across the area of interest (256 × 200 pixels). A complete CL spectrum as function of wavelength λ is recorded and stored at each pixel (x, y) together with the signal from the secondary-electron detector, providing a correlation of surface topology and optoelectronic properties. The resulting 3D dataset $I_{CL}(x, y, \lambda)$ can be evaluated *ex situ* to produce local CL spectra, CL line scans as well as CL wavelength images, i.e., a mapping of the local emission wavelength at each sample position.

Figure 13 shows a CL spectrum line scan extracted across a cross-section sample. Within the Cu(In,Ga)Se_2 thin film, the spectra are dominated by two separate emission lines around 1,040 and 1,140 nm. Beyond these lines, only the high energy peak is visible. This peak shifts clearly with decreasing distance to the surface of the Cu(In,Ga)Se_2 layer. This shift can be correlated directly to a compositional gradient along the growth direction if no strain (Siegle et al., 1997), no internal fields (Pal et al., 1994), and no charge carrier concentration gradients (Schubert et al., 1997), which all have a slight effect on the luminescence, are taken into account. These restrictions make the interpretation of the peak shift rather difficult, and thus, it is not further evaluated in the present work. However, the peak shift can be correlated qualitatively to changes in the local Ga concentration across the Cu(In,Ga)Se_2 layer.

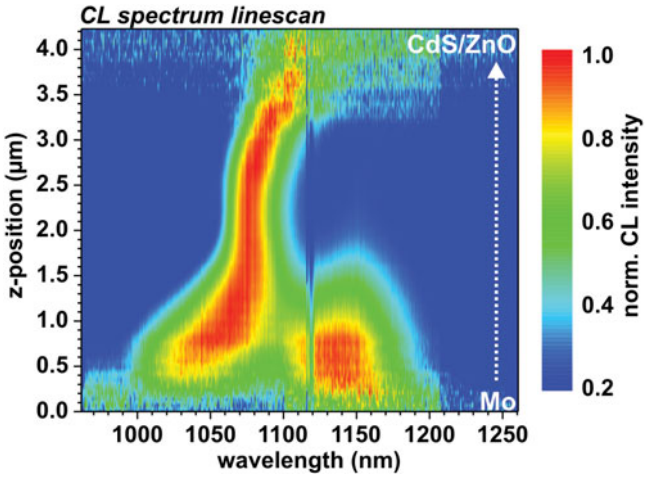

Figure 13. CL spectrum line scan across the cross section of a ZnO/CdS/Cu(In,Ga)Se_2/Mo/glass sample. The normalized CL intensities are given as false colors.

The $Cu(In,Ga)Se_2$ layer of the sample has a thickness of approximately 2 μm but appears much thicker in Figure 13. This is due to the excitation conditions during this specific measurement. A relatively high acceleration voltage and beam current led to an enlargement of the Bethe range and therefore to a reduction of the spatial resolution. The distortion around 1,120 nm is an artifact caused by the detector.

Electron Energy-Loss Spectroscopy and Energy-Filtered Transmission Electron Microscopy

Transmission electron microscopy provides several techniques for elemental distribution analysis. Apart from TEM-EDX, also electron energy-loss spectroscopy (EELS) and energy-filtered transmission electron microscopy (EFTEM) (Egerton, 1996) can be employed for this task. The energy-loss spectrum of electrons that travel through the specimen and interact with the sample atoms and charge carriers therein exhibits several features from which information on elemental distributions may be deduced. Mostly, element-specific core-loss edges are evaluated for compositional analysis at the angstroms and nowadays even at the subangstrom range. Using only electrons for imaging that exhibit loss energies according to a defined core-loss edge (energy-filtered imaging) allows for the mapping of the corresponding elemental distribution.

Apart from the core-loss edge positions, the fine structures close to the edges also can be evaluated to extract information on chemical bonding (similar to XPS, also corresponding to X-ray absorption near-edge spectroscopy) and near-range ordering (equivalent to extended X-ray absorption fine structure).

The difficulty for the application of EELS or EFTEM on the matrix elements of $Cu(In,Ga)Se_2$ is the rather large loss energies of the corresponding core-loss edges, resulting in low signal-to-noise ratios. Also, the Cu-$L_{2,3}$ edge superimposes in part the Ga-$L_{2,3}$ edge. In the literature, there are few reports on EELS/EFTEM applications on $Cu(In,Ga)Se_2$ solar cells, most of them concerning elemental distributions between $Cu(In,Ga)(S,Se)_2$ and window layers alternative to CdS (Saez-Araoz et al., 2009; Törndahl et al., 2009).

It should be noted that an EEL spectrum also contains other energy-loss regions to be evaluated. Peaks in the low-loss region originating from interactions with plasmons are phase specific (Sigle et al., 2003). Also, the energy loss from valence electrons can be used to map the local band-gap energies in the thin film (Gu et al., 2010), which can be related to the local $CuInSe_2$/$CuGaSe_2$ phase compositions and thus to the distribution of the Ga concentration.

Conclusions

The present work compares 18 different techniques in their ability to analyze the elemental distributions of the matrix elements in $Cu(In,Ga)Se_2$ thin films used as absorbers in thin-film solar cells. None of these techniques can be identified as suitable for an unambiguous and quantitative elemental distribution analysis of a thin film with unknown compositional in-depth distribution. In all cases, at least two of these should be combined to enhance the quality of the analysis. Also, qualitative elemental distributions may be quantified by relating the average signal intensity distributions with elemental concentrations obtained by integral measurements, e.g., by means of XRF. Each technique has its advantages, which are helpful for the specific requirements of an analysis, and certain disadvantages, which need to be compensated by the employment of further methods when aiming for unambiguous measurement results.

Acknowledgments

The authors are grateful to N. Blau, B. Bunn, C. Kelch, M. Kirsch, P. Körber, and T. Münchenberg for help in solar-cell production. Continuous help in sample preparation by U. Bloeck and P. Schubert-Bischoff is also gratefully acknowledged. The IFW Dresden group would like to thank Spectruma Analytik GmbH, Hof, Germany for their instrumental support. Special thanks are due to S. Zaefferer, MPI for Iron Research, Düsseldorf, to A.J. Wilkinson, University of Oxford, and to D.-V. Hodoroaba, BAM Berlin, for valuable discussions on the possibilities and limitations of EBSD and microanalysis techniques.

References

Abou-Ras, D., Dietrich, J., Kavalakkatt, J., Nichterwitz, M., Schmidt, S.S., Koch, C.T., Caballero, R., Klaer, J. & Rissom, T. (2011). Analysis of $Cu(In,Ga)(S,Se)_2$ thin-film solar cells by means of electron microscopy. *Sol Energ Mater Sol C* **95**, 1452–1462.

Abou-Ras, D., Rudmann, D., Kostorz, G., Spiering, S., Powalla, M. & Tiwari, A.N. (2005). Microstructural and chemical studies of interfaces between $Cu(In,Ga)Se_2$ and In_2S_3 layers. *J Appl Phys* **97**, 084908-1–084908-8.

Alonso, M.I., Wakita, K., Pascual, J., Garriga, M. & Yamamoto, N. (2001). Optical functions and electronic structure of $CuInSe_2$, $CuGaSe_2$, $CuInS_2$, and $CuGaS_2$. *Phys Rev B* **63**, 075203-1–075203-13.

Álvarez-García, J., Pérez-Rodríguez, A., Romano-Rodríguez, A., Morante, J.R., Calvo-Barrio, L., Scheer, R. & Klenk, R. (2001). Microstructure and secondary phases in coevaporated $CuInS_2$ films: Dependence on growth temperature and chemical composition. *J Vac Sci Technol A* **19**, 232–239.

Angeli, J., Bengtson, A., Bogaerts, A., Hoffmann, V., Hodoroaba, V.-D. & Steers, E.B.M. (2003). Glow discharge optical emission spectrometry: Moving towards reliable thin film analysis–a short review. *J Anal At Spectrom* **18**, 670–679.

Barkshire, I., Karduck, P., Rehbach, W.P. & Richter, S. (2000). High-spatial-resolution low-energy electron beam X-ray microanalysis. *Mikrochim Acta* **132**, 113–128.

Beckhoff, B. (2008). Reference-free X-ray spectrometry based on metrology using synchrotron radiation. *J Anal At Spectrom* **23**, 845–853.

Bengtson, A. (1994). Quantitative depth profile analysis by glow discharge. *Spectrochim Acta, Part B: Atomic Spectroscopy* **49**, 411–429.

Bergmaier, A., Dollinger, G. & Frey, C.M. (1995). Quantitative elastic recoil detection. *Nucl Instrum Meth Phys Res B* **99**, 488–490.

Bergmaier, A., Dollinger, G. & Frey, C.M. (1998). A compact Δ/E-E_{res} detector for elastic recoil detection with high sensitivity. *Nucl Instrum Meth Phys Res B* **136–138**, 638–643.

Boccara, A.C., Pickering, C. & Rivory, J. (Eds.) (1993). *Proceedings of the First International Conference on Spectroscopic Ellipsometry*, Paris, France, January 11–14, 1993, *Thin Solid Films* **234**.

Bohne, W., Röhrich, J., Schöpke, A., Selle, B., Sieber, I., Fuhs, W., del Prado, A., San Andrés, E., Mártil, I. & González-Díaz, G. (2004). Compositional analysis of thin SiO_xN_y:H films by heavy-ion ERDA, standard RBS, EDX and AES: A comparison. *Nucl Instrum Meth Phys Res B* **217**, 237–245.

Caballero, R., Izquierdo-Roca, V., Fontané, X., Kaufmann, C.A., Álvarez-García, J., Eicke, A., Calvo-Barrio, L., Pérez-Rodríguez, A., Schock, H.W. & Morante, J.R. (2010). Cu deficiency in multi-stage co-evaporated Cu(In,Ga)Se_2 for solar cells applications: Microstructure and Ga in-depth alloying, *Acta Mater* **58**, 3468–3476.

Cadel, E., Barreau, N., Kessler, J. & Pareige, P. (2010). Atom probe study of sodium distribution in polycrystalline Cu(In, Ga)Se_2 thin film. *Acta Mater* **58**, 2634–2637.

Cahen, D. & Noufi, R. (1992). Free energies and enthalpies of possible gas phase and surface reactions for preparation of $CuInSe_2$. *J Chem Phys Solids* **53**(8), 991–1005.

Chakrabarti, R., Maity, A.B., Maiti, B., Dutta, J., Chaudhuri, S. & Pal, A.K. (1996). Effect of Ga incorporation in polycrystalline $CuInSe_2$ films. *Vacuum* **47**, 1371–1378.

Chakrabarti, R., Maity, A.B., Pal, R., Bhattacharyya, D., Chaudhuri, S. & Pal, A.K. (1997). Estimation of stress in polycrystalline $CuInSe_2$ films deposited on Mo-coated glass substrates. *Phys Stat Sol (a)* **160**, 67–76.

Chu, W.K., Mayer, J.W. & Nicolet, M.A. (1978). *Backscattering Spectrometry*. Orlando, FL: Academic Press.

Collins, R.W., Aspnes, D.E. & Irene, E.A. (Eds.) (1998). *Proceedings of the Second International Conference on Spectroscopic Ellipsometry*, Charleston, South Carolina, May 12–15, 1997, *Thin Solid Films* **313–314**.

Collins, R.W. & Ferlauto, A.S. (2005). Optical physics of materials. In *Handbook of Ellipsometry*, Tompkins, H.G. & Irene, E.A. (Eds.), pp. 93–236. Norwich, NY: William Andrew Publishing.

Doolittle, L.R. (1986). A semiautomatic algorithm for Rutherford backscattering analysis. *Nucl Instrum Meth B* **15**, 227–231.

Dullweber, T., Rau, U., Contreras, M.A., Noufi, R. & Schock, H.W. (2000). Photogeneration and carrier recombination in graded gap Cu(In,Ga)Se_2 solar cells. *IEEE Trans Electron Dev* **47**, 2249–2254.

Egerton, R.F. (1996). *Electron Energy-Loss Spectroscopy in Electron Microscopy*. New York: Plenum Press.

Escobar Galindo, R., Gago, R., Lousa, A. & Albella, J.M. (2009). Comparative depth-profiling analysis of nanometer-metal multilayers by ion-probing techniques. *Trends Anal Chem* **28**, 494–505.

Fernández, B. & Wasim, S.M. (1990). Sound velocities and elastic moduli in $CuInTe_2$ and $CuInSe_2$. *Phys Status Solidi A* **122**, 235–242.

Firoz Hasan, S.M., Quadir, L., Begum, K.S., Subhan, M.A. & Mannan, K.M. (1999). Analysis of the optical absorption characteristics of $CuInSe_2$ thin films. *Sol Energ Mat Sol Cells* **58**, 349–360.

Fujiwara, H., Koh, J., Rovira, P.I. & Collins, R.W. (2000). Assessment of effective-medium theories in the analysis of nucleation and microscopic surface roughness evolution for semiconductor thin films. *Phys Rev B* **61**, 10832–10844.

Fujiwara, H., Koh, J., Wronski, C.R., Collins, R.W. & Burnham, J.S. (1998). Optical depth profiling of band gap engineered interfaces in amorphous silicon solar cells at monolayer resolution. *Appl Phys Lett* **72**, 2993–2995.

Gabor, A.M., Tuttle, J.R., Schwartzlander, A., Tennant, A.L., Contreras, M.A. & Noufi, R. (1994). Band-gap engineering in Cu(In,Ga)Se_2 thin films grown from $(In,Ga)_2Se_3$ precursors. In *Conference Record of the 1st World Conference on Photovoltaic Energy Conversion*, Waikoloa, Hawai'i, December 5–9, 1994, pp. 83–86. Piscataway, NJ: IEEE.

Gault, B., Vurpillot, F., Vella, A., Gilbert, M., Menand, A., Blavette, D. & Deconihout, B. (2006). Design of a femtosecond laser assisted tomographic atom probe. *Rev Sci Instrum* **77**, 043705-1–043705-8.

Granata, J.E. & Sites, J.R. (1998). Impact of sodium in the bulk and in grain boundaries of $CuInSe_2$. *Proceedings of the 2nd World Conference and Exhibition on Photovoltaic Energy Conversion*, Vienna, Austria, July 6–10, 1998, Schmid, J., Ossenbrink, H.A., Helm, P., Ehmann, H. & Dunlop, E.D. (Eds.), pp. 604–607. Luxembourg: Office for Official Publications of the European Communities.

Gu, L., Özdöl, V.B., Sigle, W., Koch, C.T., Srot, V. & van Aken, P.A. (2010). Correlating the structural, chemical, and optical properties at nanometer resolution. *J Appl Phys* **107**, 013501-1–013501-4.

Herberholz, R., Rau, U., Schock, H.W., Haalboom, T., Gödecke, T., Ernst, F., Beilharz, C., Benz, K.W. & Cahen, D. (1999). Phase segregation, Cu migration and junction formation in Cu(In, Ga)Se_2. *Eur Phys J Appl Phys* **6**, 131–139.

Hodoroaba, V.-D., Unger, E.S.U., Jenett, H., Hoffmann, V., Hagenhoff, B., Kayser, S. & Wetzig, K. (2001). Depth profiling of electrically non-conductive layered samples by RF-GDOES and HFM plasma SNMS. *Appl Surf Sci* **179**, 30–37.

Ives, M., Lewis, D.B. & Lehmberg, C. (1997). Depth profile analysis of multilayer Ni–Fe alloy coatings by glow discharge optical emission spectroscopy (GDOES) and energy dispersive X-ray (EDX) linescan—A comparative study. *Surf Interf Anal* **25**, 191–201.

Jackson, P., Hariskos, D., Lotter, E., Paetel, S., Wuerz, R., Menner, R., Wischmann, W. & Powalla, M. (2011). New world record efficiency for Cu(In,Ga)Se_2 thin-film solar cells beyond 20%. *Prog Photovoltaics Res Appl* doi:10.1002/pip.1078.

Johs, B., Hale, J., Ianno, N.J., Herzinger, C.M., Tiwald, T. & Woollam, J.A. (2001). Recent developments in spectroscopic ellipsometry for *in situ* applications. In *Optical Metrology Roadmap for the Semiconductor, Optical, and Data Storage Industries II*, Duparré, A. & Singh, B. (Eds.), Vol. 4449, pp. 41–57. Bellingham, WA: SPIE Publishing.

Kacher, J., Landon, C., Adams, B.L. & Fullwood, D. (2009). Bragg's Law diffraction simulations for electron backscatter diffraction analysis. *Ultramicroscopy* **109**, 1148–1156.

Kaufmann, C.A., Caballero, R., Unold, T., Hesse, R., Klenk, R., Schorr, S., Nichterwitz, M. & Schock, H.-W. (2009). Depth profiling of Cu(In,Ga)Se_2 thin films grown at low temperatures. *Sol En Mat Sol Cells* **93**, 859–863.

Kaufmann, C.A., Neisser, A., Klenk, R. & Scheer, R. (2005). Transfer of Cu(In,Ga)Se_2 thin film solar cells to flexible sub-

strates using an *in situ* process control. *Thin Solid Films* **480–481**, 515–519.

Kelly, T. & Miller, M.K. (2007). Atom probe tomography. *Rev Sci Instrum* **78**, 031101-1–031101-20.

Klenk, R., Walter, T., Schock, H.W. & Cahen, D. (1993). A model for the successful growth of polycrystalline films of $CuInSe_2$ by multisource physical vacuum evaporation. *Adv Mater* **5**, 114–119.

Kötschau, I.M. & Schock, H.W. (2003). Depth profile of the lattice constant of the Cu-poor surface layer in $(Cu_2Se)_{1-x}(In_2Se_3)_x$ evidenced by grazing incidence X-ray diffraction. *J Phys Chem Solids* **64**, 1559–1563.

Kötschau, I.M. & Schock, H.W. (2006). Compositional depth profiling of polycrystalline thin films by grazing-incidence X-ray diffraction. *J Appl Cryst* **39**, 683–696.

L'Ecuyer, J.L., Brassard, C., Cardinal, C., Chabbal, J., Deschênes, L., Labrie, J.P., Terreault, B., Martel, J.G. & St.-Jacques, R. (1976). An accurate and sensitive method for the determination of the depth distribution of light elements in heavy materials. *J Appl Phys* **47**, 381–382.

Lee, J., Rovira, P.I., An, I. & Collins, R.W. (1998). Rotating compensator multichannel ellipsometry: Applications for real time Stokes vector spectroscopy of thin film growth. *Rev Sci Instrum* **69**, 1800–1810.

Levenberg, K. (1944). A method for the solution of certain problems in least squares. *Quart Appl Math* **2**, 164–168.

Marquardt, D. (1963). An algorithm for least-squares estimation of nonlinear parameters. *SIAM J Appl Math* **11**, 431–441.

Marsillac, S., Ranjan, V. & Little, S. (2010). *In-situ* study of $Cu(In,Ga)Se_2$ dielectric functions evolution as a function of copper content. In *Conference Record of the 35th IEEE Photovoltaic Specialists Conference*, Honolulu, USA, June 20–25, 2010. Piscataway, NJ: IEEE.

Miller, M.K. (2000). *Atom Probe Tomography—Analysis at the Atomic Level*. New York: Kluwer Academic/Plenum Publishers.

Mönig, H., Fischer, C.-H., Grimm, A., Johnson, B., Kaufmann, C.A., Caballero, R., Lauermann, I. & Lux-Steiner, M.C. (2010). Surface Cu-depletion of $Cu(In,Ga)Se_2$ thin films: Further experimental evidence for a defect-induced surface reconstruction. *J Appl Phys* **107**, 113540-1–113540-5.

Mönig, H., Lauermann, I., Grimm, A., Camus, C., Kaufmann, C.A., Pistor, P., Jung, C., Kropp, T., Lux-Steiner, M.C. & Fischer, C.-H. (2008). Controlled variation of the information depth by angle dependent soft X-ray emission spectroscopy: A study on polycrystalline $Cu(In,Ga)Se_2$. *Appl Surf Sci* **255**, 2474–2477.

Niles, D.W., Ramanathan, K., Hasoon, F., Noufi, R., Tielsch, B.J. & Fulghum, J.E. (1997). Na impurity chemistry in photovoltaic $Cu(In,Ga)Se_2$ thin films: Investigation with X-ray photoelectron spectroscopy. *J Vac Sci Techn A* **15**, 3044–3049.

Oechsner, H. (Ed.) (1984). *Thin Film and Depth Profile Analysis, Topics in Current Physics*, vol. 37. Berlin: Springer.

Pal, R., Chattopadhyay, K.K., Chaudhuri, S. & Pal, A.K. (1994). Variation of trap state density and barrier height with Cu/In ratio in $CuInSe_2$ films. *Thin Solid Films* **247**, 8–14.

Payling, R. & Jones, D.G. (1993). Fundamental parameters in quantitative depth profiling and bulk analysis with glow discharge spectrometry. *Surf Interf Anal* **20**, 787–795.

Platzer-Björkman, C., Törndahl, T., Abou-Ras, D., Malmström, U., Kessler, J. & Stolt, L. (2006). Zn(O,S) buffer layers by atomic layer deposition in $Cu(In,Ga)Se_2$ based thin film solar cells: Band alignment and sulfur gradient. *J Appl Phys* **100**, 044506-1–044506-9.

Podraza, N.J., Li, J., Wronski, C.R., Dickey, E.C., Horn, M.W. & Collins, R.W. (2008). Analysis of $Si_{1-x}Ge_x$:H thin films with graded composition and structure by real time spectroscopic ellipsometry. *Phys Stat Sol A* **205**, 892–895.

Reniers, F. & Tewell, C.R. (2009). In depth analysis (profiling). In *Handbook of Surface and Interface Analysis, Methods for Problem-Solving*, 2nd ed., Rivière, J.C. & Myhra, S. (Eds.), pp. 281–318. London: Taylor & Francis Group.

Rincón, C. & Ramírez, F.J. (1992). Lattice vibrations of $CuInSe_2$ and $CuGaSe_2$ by Raman microspectrometry. *J Appl Phys* **72,** 4321–4324.

Rockett, A., Britt, J.S., Gillespie, T., Marshall, C., Al Jassim, M.M., Hasoon, F., Matson, R. & Basol, B. (2000). Na in selenized $Cu(In,Ga,Se)_2$ on Na-containing and Na-free glasses: Distribution, grain structure, and device performances. *Thin Solid Films* **372**, 212–217.

Saez-Araoz, R., Abou-Ras, D., Niesen, T.P., Neisser, A., Wilchelmi, K., Lux-Steiner, M.Ch. & Ennaoui, A. (2009). *In situ* monitoring the growth of thin-film ZnS/Zn(S,O) bilayer on Cu-chalcopyrite for high performance thin film solar cells. *Thin Solid Films* **517**, 2300–2304.

Schlesinger, R., Oberdorfer, C., Würz, R., Greiwe, G., Stender, P., Artmeier, M., Pelka, P., Spaleck, F. & Schmitz, G. (2010). Design of a laser-assisted tomographic atom probe at Münster University. *Rev Sci Instrum* **81**, 043703-1–043703-8.

Schmid, T., Camus, C., Lehmann, S., Abou-Ras, D., Fischer, C.-H., Lux-Steiner, M.C. & Zenobi, R. (2009). Spatially resolved characterization of chemical species and crystal structures in $CuInS_2$ and $CuGa_xSe_y$ thin films using Raman microscopy. *Phys Stat Sol A* **206**, 1013–1016.

Schubert, E.F., Goepfert, I.D., Grieshaber, W. & Redwing, J.M. (1997). Optical properties of Si-doped GaN. *Appl Phys Lett* **71**, 921–923.

Siegle, H., Hoffmann, A., Eckey, L., Thomsen, C., Christen, J., Bertram, F., Schmidt, D., Rudloff, D. & Hiramatsu, K. (1997). Vertical strain and doping gradients in thick GaN layers. *Appl Phys Lett* **71**, 2490–2492.

Sigle, W., Kramer, S., Varshney, V., Zern, A., Eigenthaler, U. & Rühle, M. (2003). Plasmon energy mapping in energy-filtering transmission electron microscopy. *Ultramicroscopy* **96**, 565–571.

Stephan, C., Schorr, S. & Schock, H.-W. (2009). New structural investigations in the $Cu_2Se(S)$-$In_2Se_3(S)$/$Cu_2Se(S)$-$Ga_2Se_3(S)$ phase diagrams. In *Thin-Film Compound Semiconductor Photovoltaics—2009*, Yamada, A., Heske, C., Contreras, M., Igalson, M. & Irvine, S.J.C. (Eds.), *MRS Symp Proc* **1165**, 1165-M09-08-1–6. Warrendale, PA: Materials Research Society.

Streeck, C., Beckhoff, B., Reinhardt, F., Kolbe, M., Kanngiesser, B., Kaufmann, C.A. & Schock, H.W. (2010). Elemental depth profiling of $Cu(In,Ga)Se_2$ thin films by reference-free grazing incidence X-ray fluorescence analysis. *Instrum Meth Phys Res B* **268**, 277–281.

Suri, D.K., Nagpal, K.C. & Chadha, G.K. (1989). X-ray study of $CuGa_xIn_{1-x}Se_2$ solid solutions. *J Appl Crystallogr* **22**, 578–583.

Tanino, H., Deai, H. & Nakanishi, H. (1993). Raman spectra of $CuGa_xIn_{1-x}Se_2$. *Jpn J Appl Phys* **32**(Suppl 32–3), 436–438.

Thompson, K., Lawrence, D., Larson, D.J., Olson, J.D., Kelly, T.F. & Gorman, B. (2007). *In situ* site-specific specimen preparation for atom probe tomography. *Ultramicroscopy* **107**, 131–139.

Törndahl, T., Coronel, E., Hultqvist, A., Platzer-Björkman, C., Leifer, K. & Edoff, M. (2009). The effect of $Zn_{1-x}Mg_xO$

buffer layer deposition temperature on $Cu(In,Ga)Se_2$ solar cells: A study of the buffer/absorber interface. *Prog Photovoltaics Res Appl* **17**, 115–125.

Walker, J.D., Khatri, H., Ranjan, V., Little, S., Zartman, R., Collins, R.W. & Marsillac, S. (2009). Dielectric functions and growth dynamics of $CuIn_{1-x},Ga_xSe_2$ absorber layers via *in situ* real time spectroscopic ellipsometry. In *Conference Record of the 34th IEEE Photovoltaics Specialists Conference*, Philadelphia, Pennsylvania, June 7–12, 2009, pp. 1154–1156. Piscataway, NJ: IEEE.

Watanabe, M., Ackland, D.W., Burrows, A., Kiely, C.J., Williams, D.B., Krivanek, O.L., Dellby, N., Murfitt, M.F. & Szilagyi, Z. (2006). Improvements in the X-ray analytical capabilities of a scanning transmission electron microscope by spherical-aberration correction. *Microsc Microanal* **12**, 515–526.

Wilkinson, A.J., Meaden, G. & Dingley, D.J. (2006*a*). High-resolution elastic strain measurement from electron backscatter diffraction patterns: New levels of sensitivity. *Ultramicroscopy* **106**, 307–313.

Wilkinson, A.J., Meaden, G. & Dingley, D.J. (2006*b*). High resolution mapping of strains and rotations using electron backscatter diffraction. *Mat Sci Techn* **22**(11), 1271–1278.

Witte, W., Kniese, R. & Powalla, M. (2009*a*). Raman investigations of $Cu(In,Ga)Se_2$ thin films with various copper contents. *Thin Solid Films* **517**, 867–869.

Witte, W., Kniese, R. & Powalla, M. (2009*b*). Influence of the Cu content on structural and vibrational properties in polycrystalline $CuGaSe_2$ thin films. In *Thin-Film Compound Semiconductor Photovoltaics—2009*, Yamada, A., Heske, C., Contreras, M., Igalson, M. & Irvine, S.J.C. (Eds.), *MRS Symp. Proc.* **1165**, 1165-M05-20-1–1165-M05-20-6. Warrendale, PA: Materials Research Society.

Zaefferer, S. (2002). Computer aided crystallographic analysis in the TEM. *Adv Imag Electr Phys* **125**, 355–415.